

Line formation in the inner winds of classical T Tauri stars: testing the conical-shell wind solution

Ryuichi Kurosawa^{*} and M. M. Romanova

Department of Astronomy, Cornell University, Space Sciences Building, Ithaca, NY 14853-6801, USA

Dates to be inserted

ABSTRACT

We present the emission line profile models of hydrogen and helium based on the results from axisymmetric magnetohydrodynamics (MHD) simulations of the wind formed near the disk-magnetosphere boundary of classical T Tauri stars (CTTSs). We extend the previous outflow models of ‘the conical-shell wind’ by Romanova et al. to include a well defined magnetospheric accretion funnel flow which is essential for modelling the optical and near-infrared hydrogen and helium lines of CTTSs. The MHD model with an intermediate mass-accretion rate shows outflows in conical-shell shape with a half opening angle $\sim 35^\circ$. The flow properties such as the maximum outflow speed in the conical-shell wind, maximum inflow speed in the accretion funnel, mass-accretion and mass-loss rates are comparable to those found in a typical CTTS. The density, velocity and modified temperature from the MHD simulations are used in a separate radiative transfer model to predict the line profiles and test the consistency of the MHD models with observations. The line profiles are computed with various combinations of X-ray luminosities, temperatures of X-ray emitting plasma, and inclination angles. A rich diversity of line profile morphology is found, and many of the model profiles are very similar to those found in observations. We find that the conical-shell wind may contribute to the emission in some hydrogen lines (e.g. H α , H β , Pa β and Pa γ) significantly when the temperature in the wind is relatively high (e.g. $\sim 10^4$ K); however, the wind contribution decreases rapidly when a lower wind temperature is adopted. The model well reproduces a relatively narrow and low-velocity blueshifted absorption component in He I $\lambda 10830$, which are often seen in observations.

Key words: line: formation – stars: low-mass, brown dwarfs – stars: pre-main-sequence – stars: winds, outflows – MHD

1 INTRODUCTION

Mass outflows are commonly found during mass accreting phases of pre-main-sequence stars. While powerful collimated outflows are observed in protostars, often less collimated and weaker outflows are associated with classical T Tauri stars (CTTSs) (e.g. Ray et al. 2007). The outflows in CTTSs are most likely powered by accretion processes, as the strengths of mass outflow indicators are known to correlate with those of mass accretion (e.g. Cabrit et al. 1990; Hartigan, Edwards, & Ghandour 1995). Understanding the origin and properties of the wind from young stellar objects is very important as it is closely related to their spin and disc evolutions. The mass-loss process is one of the key mechanisms through which YSOs can remove their angular momentum to the surrounding environment during the active accretion phases (e.g. Hartmann & Stauffer 1989; Königl 1991; Shu et al. 1994; Matt & Pudritz 2005; 2007; 2008).

The outflows in the low-mass stars such as CTTSs are unlikely driven by thermally or radiatively due to their relatively low temperature and luminosity. On other hand, relatively large magnetic field strengths ($\sim 10^3$ G) are found in CTTSs (e.g. Johns-Krull et al. 1999; Symington et al. 2005b; Donati J.-F. et al. 2007; Donati J.-F. et al. 2008) which supports an idea that the wind is formed in magnetohydrodynamics processes (Königl, Romanova, & Lovelace 2011). The recent magnetohydrodynamics (MHD) simulation of Romanova et al. (2009) (hereafter RO09) showed a new type of outflow solution, so-called ‘the conical-shell wind’, which is produced when the stellar dipole magnetic field is compressed by the accretion disc into the X-wind (Shu et al. 1994) like configuration. The resulting outflow occurs in rather narrow conical-shell shapes with their half opening angles between 30° to 40° . This conical-shell wind is similar to the X-wind of Shu et al. (1994) in which the wind launching region is restricted to a narrow region near the inner edge of the accretion disc around the corotation radius. However, unlike the X-wind model, the conical-shell wind model of RO09 does not require the magnetospheric radius to

* E-mail:kurosawa@astro.cornell.edu

be matched with the corotation radius of the system. More recent simulations performed with larger radial domains have shown that the conical-shell winds become strongly collimated by the magnetic force at larger distances (Lii, Romanova, & Lovelace 2012). The model has been also applied to the higher mass-accretion rate FU Orionis systems (FUORs) Königl et al. (2011). Other possible wind configurations often considered for the outflows in CTTSSs (e.g. Ferreira, Dougados, & Cabrit 2006) are: (1) a disc wind, which requires a sufficient magnetic field and ionization fraction to launch magnetocentrifugal winds over a relatively wide range of disk radii (e.g. Ustyugova et al. 1995; Romanova et al. 1997; Ouyed & Pudritz 1997; Ustyugova et al. 1999; Königl & Pudritz 2000; Krasnopol'sky, Li, & Blandford 2003; Pudritz et al. 2007), and (3) a stellar wind in which outflows occurs along the open magnetic fields from the stellar surface (e.g., Hartmann, Avrett, & Edwards 1982; Kwan & Tademaru 1988; Hirose et al. 1997; Romanova et al. 2005; Cranmer 2009).

Spectroscopic studies of strong emission lines in CTTSSs may be able to constrain the launching regions of the winds. This, in turn, would restrict possible wind formation theories mentioned above. A usefulness of the optically thick He I $\lambda 10830$ as a diagnostic of the inner wind from the accreting stars has been demonstrated in the observations by e.g. Takami et al. (2002), Edwards et al. (2003), Dupree et al. (2005), Edwards et al. (2006) (hereafter ED06) and Podio et al. (2008). In particular, ED06 showed that a very high fraction (~ 70 per cent) of CTTSSs exhibit a blueshifted absorption (below the continuum), which is clear sign of outflow. This is much higher than the rate found in another wind sensitive line, H α , for which only about 10 per cent of stars exhibit a similar type of blueshifted absorption component (below the continuum) (e.g., Reipurth, Pedrosa, & Lago 1996). Edwards (2007) and Kwan, Edwards, & Fischer (2007) suggested that the blueshifted absorption component in the He I $\lambda 10830$ profiles is caused by a stellar wind in about 40 per cent, and by a disc wind in about 30 per cent of the samples in ED06. Using local excitation calculations combined with spectroscopic observations, Kwan & Fischer (2011) also demonstrated the effectiveness of He I $\lambda 10830$ for probing the density and temperature of the inner wind. The signs for the inner winds are also seen blueshifted absorption component in Na D, Ca II (H and K), and Mg II (*h* and *k*) (e.g. Calvet 1997; Ardila et al. 2002); however, probing the launching regions using these lines are more difficult (ED06).

Previously, we have developed and tested a multidimensional non-LTE radiative transfer model of hydrogen and helium line profiles, which uses the Sobolev approximation in the source function calculations (Kurosawa, Romanova, & Harries 2011, hereafter KU11; see also Harries 2000; Kurosawa, Harries, & Symington 2006). The model uses rather simple kinematic and geometric models for both stellar and disc winds (see also Hartmann et al. 1990; Calvet, Hartmann, & Hewett 1992). We demonstrated that our models are consistent with the scenario in which the narrow blueshifted absorption component of He I $\lambda 10830$ seen in observations is caused by a disc wind, and the wider blueshifted absorption component (the P-Cygni profile) is caused by a bipolar stellar wind. Similar conclusions were reached in the earlier study by Kwan et al. (2007) who also applied simple kinematic and geometric wind models. To advance our understanding of the line formations in the inner wind of CTTSSs, we now apply our model to more realistic wind configurations such as those found in MHD simulations. Therefore, our main goals in this paper are to present the optical and near-infrared hydrogen and helium line profile models computed with the density, velocity and modified temperature (Sec-

tion 5.1) from the conical-shell wind solution found in the MHD simulations of RO09, and to check the consistency of the wind solution with observed line profiles.

In Section 2, the model assumption and setup of our MHD simulations are presented, and those for the radiative transfer model for computing line profiles are given in Section 3. The results of the MHD simulations and the line profiles models are summarised in Sections 4 and 5, respectively. Brief discussions in which the line profile models are compared with observations are given in Section 6. Finally main findings and conclusions are summarised in Section 7.

2 MHD MODEL

The numerical method and the code used to simulate the outflow from the disk-magnetosphere interaction region are essentially identical to those in the conical-shell wind models of Romanova et al. (2009) (hereafter RO09; see also Ustyugova et al. 2006); hence, we briefly describe only the most important aspects of our numerical MHD simulations below.

2.1 Outline

The simulation domain is divided into two regions: (1) the accretion disc region and (2) the corona region which are located outside of the disc region. The former is described by the equations of viscous and resistive MHD, and the latter by those of ideal MHD. The plasma is assumed to be an ideal gas with adiabatic index $\gamma = 5/3$. We adopt the standard α prescriptions of Shakura & Sunyaev (1973) for the coefficient of the turbulent kinematic viscosity $\nu_t \equiv \alpha_v c_s^2 / \Omega_K$, where c_s , Ω_K , α_v are the isothermal sound speed, the Keplerian angular velocity, and the dimensionless viscosity coefficient, respectively. Similarly, the turbulent magnetic diffusivity coefficient is defined as $\eta_t \equiv \alpha_d c_s^2 / \Omega_K$ where α_d are the dimensionless turbulent diffusivity coefficient. Both, viscosity and diffusivity correspond to some type of turbulence in the disc; hence, they are included only in the disc which is distinguished from the low-density corona. Thus, we set $\alpha_v, \alpha_d = 0$ when the density is lower than a typical density in the disc (ρ_d), i.e. when $\rho < \rho_d$. The viscosity term helps to bring matter towards the star in a steady rate, while diffusivity helps this matter to diffuse through the magnetic field lines of the magnetosphere. We refer to RO09 and Lii et al. (2012) for more comprehensive descriptions of our implementations of the stress tensor, viscosity and diffusivity.

The MHD equations are solved numerically by using the Godunov-type conservative code described in detail in RO09 and Ustyugova et al. (2006). The code uses the spherical coordinates (r, θ, ϕ) where θ and ϕ are the polar and azimuthal angles. We consider axisymmetric approximation, i.e. $\partial/\partial\phi = 0$.

2.2 Initial and boundary conditions

The initial configuration of the magnetic field is set by a dipole field aligned with the stellar spin axis, i.e.

$$\mathbf{B} = [3(\boldsymbol{\mu} \cdot \mathbf{r})\mathbf{r} - \boldsymbol{\mu} r^2]/r^5, \quad (1)$$

where $\boldsymbol{\mu}$ is the magnetic dipole moment of the star. The simulation domain is initialised with a low-density, high-temperature plasma (corona) which is described as the following density and pressure distributions: $\rho = \rho_c \exp[GM_*/(\mathcal{R}T_c r)]$ and $p =$

$p_c \exp[GM_*/(\mathcal{R}T_c r)]$ where T_c , ρ_c and p_c are the temperature, density and pressure at the outer boundary, respectively. The symbols G and M_* are the gravitational constant and the stellar mass. The initial velocity of the corona is set to zero everywhere. The outer boundary $r = R_{\text{out}}$ are divided into a disc region $\theta_d \leq \theta \leq \pi/2$, and a corona region $0 \leq \theta < \theta_d$ with $\theta_d \approx 65^\circ$. At the beginning of the simulation ($t = 0$), there is no high density disc matter in the domain. We fix the density and temperature in the disc region at the outer boundary to $\rho = \rho_d$ and $T = T_d$. Consequently as the simulation advances in time, a high-density (ρ_d) low-temperature (T_d) gas enters the simulation domain through the disc boundary region, $\theta > \theta_d$. The gas in the disc region continues to flow inward due to the α viscosity described earlier. The spin of the central star is initially set to a small value corresponding to $r_{\text{cor}} = R_{\text{out}}$ where $r_{\text{cor}} = (GM_*/\Omega^2)^{1/3}$, and it is gradually increased to a final stellar angular velocity, Ω_* . As the simulation progresses, the information about the stellar rotation propagates rapidly to the low-density corona.

At the inner boundary ($r = R_{\text{in}}$), the frozen-in condition is applied to the poloidal component B_p of the field i.e., B_r is fixed while ‘free’ boundary conditions are applied to B_θ and B_ϕ ($\partial B_\theta / \partial r = 0$ and $\partial B_\phi / \partial r = 0$). The free boundary conditions [$\partial(\dots) / \partial r = 0$] are also applied to density, pressure, and specific entropy. The velocity components are calculated using free boundary conditions, and adjusted to be parallel to the magnetic field vector at the inner boundary. No matter enters from the inner boundary. The mass injection from the inner boundary, e.g. via a stellar wind, is not considered in this work.

At the outer boundary ($r = R_{\text{out}}$) of the corona region ($0 \leq \theta < \theta_d$), the free boundary conditions are applied to all the hydrodynamic variables. The matter is free to flow out, but no matter is allowed to enter from the outer boundary in the coronal region. At the outer boundary of the disc region, ($\theta_d \leq \theta \leq \pi/2$), the density is fixed at the ‘disc density’ (ρ_d). The velocity is fixed at a slightly sub-Keplerian velocity, i.e. $\Omega_d = \kappa\Omega(r_d)$ where $\kappa = 0.997$. This allows the matter to flow into the simulation region through the boundary more easily. Finally, the boundary conditions on the equatorial plane and on the rotation axis are symmetric and antisymmetric, respectively.

3 RADIATIVE TRANSFER MODEL

The density, velocity and modified temperature (Section 5.1) from a snapshot of the MHD model, as described above, will be used as inputs for the line profile calculations. The hydrogen and helium line profiles from the simulations are computed by using the radiative transfer code TORUS (e.g. Harries 2000; Kurosawa et al. 2006; KU11). The numerical method used in this work is essentially identical to those in KU11. Below, we briefly describe only the essential aspects of the model, and refer readers to KU11 for more comprehensive descriptions of our radiative transfer model.

3.1 Outline

The basic steps for computing the line profiles are as follows: (1) mapping of the density, velocity and temperature (but see Section 5.1), from an MHD simulation output to the radiative transfer grid, (2) the source function (S_ν) calculation and (3) the observed flux/profile calculation. A brief description of each step is described below.

In step (1), we use a mesh refinement grid which allows us an

accurate mapping of an MHD simulation data on to the radiative transfer grid. In the grid construction process, we ensure that the resolution of the radiative transfer grid is higher or equivalent to the original MHD simulation grid. In step (2), we adopt the method described by Klein & Castor (1978) (see also Rybicki & Hummer 1978; Hartmann, Hewett, & Calvet 1994) in which the Sobolev approximation method is used. Our atomic model consists of 20 bound levels for H I, 19 levels for He I (up to the principal quantum number $n = 4$ level), 10 levels for He II, and the continuum level for He III. In step (3), an observed line profile will be computed by using the source function found in step (2). The observed fluxes are computed in the cylindrical coordinates system whose symmetry axis points towards an observer. The line profiles are numerically computed via integrations of the equation of radiative transfer. The number of grid points used for a typical integration are $n_r = 180$ and $n_\phi = 100$ for the radial and azimuthal grid points, respectively. A typical number of frequency points used across a given line profiles is $n_\nu = 101$. The line broadening effects (Stark and van der Waals) are also included for some hydrogen lines (e.g. H α and H β).

3.2 Continuum sources

3.2.1 Photosphere

For all the line profile models presented in this work, we adopt stellar parameters of a typical classical T Tauri star for the central continuum source, i.e. its stellar radius $R_* = 2.0 R_\odot$ and its mass $M_* = 0.8 M_\odot$. Thus, we adopt the model atmosphere of Kurucz (1979), with the effective temperature of photosphere $T_{\text{ph}} = 4,000$ K and the surface gravity $\log g_* = 3.5$ (cgs), as the photospheric contribution to the continuum flux.

3.2.2 Hotspots

The hot spots on CTTSs are formed by the infalling gas along the magnetic field on to the stellar surface. As the gas approaches the surface, it decelerates in a strong shock, and is heated to $\sim 10^6$ K. The X-ray radiation produced in the shock will be absorbed by the gas locally, and re-emitted as optical and UV light (Calvet & Gullbring 1998; Gullbring et al. 2000) – forming the high temperature regions on the stellar surface with which the magnetic field intersects. In this study, we adopt the hot spot temperature model described by Romanova et al. (2004) in which the local hot spot luminosity is computed directly from the inflowing mass flux on the surface of the star from MHD simulations. The temperature of the hot spots is determined by the conversion of kinetic and internal energy of infalling plasma to a thermal radiation. Using the mass flux (ρv_r) at a given location on the stellar surface, one finds the corresponding thermal radiation temperature as $T_{\text{hs}} = (\rho v_r e_g^2 / \sigma)^{1/4}$ where $e_g = (v^2/2 + w)^2$. Further, ρ , v_r , v and σ are the density, the radial component of velocity, the speed of plasma, and the Stefan-Boltzmann constant, respectively. The specific enthalpy of the gas is $w = \gamma(p/\rho)(\gamma - 1)$ where γ is the adiabatic index and p is the gas pressure. We compare this temperature T_{hs} with the effective temperature of photosphere T_{ph} to determine the shape and the size of hot spots. When $T_{\text{hs}} > T_{\text{ph}}$, the location on the stellar surface is flagged as hot. For the hot surface, the total continuum flux is the sum of the blackbody radiation with T_{hs} and the flux from the model photosphere mentioned above. The contribution from the inflow gas is ignored when $T_{\text{hs}} < T_{\text{ph}}$.

3.2.3 X-ray emission

Relatively strong X-ray emission is commonly found in CTTSs, with their luminosities L_X (0.3 – 10 keV) ranging from $\sim 10^{28}$ erg s $^{-1}$ to $\sim 10^{31}$ erg s $^{-1}$ (e.g. Telleschi et al. 2007; Güdel & Telleschi 2007; Güdel M. et al. 2010). Recent studies by Kwan & Fischer (2011) and KU11 have shown that the photoionization by high energy photons, in addition to the normal continuum emission from the photosphere, is most likely needed for generating the high opacities and hence strong absorption features seen in the observed He I $\lambda 10830$ line profiles of CTTSs (e.g. ED06). As in KU11, we adopt a simplest model of the X-ray radiation here. We assume that the X-ray radiation arises uniformly from the stellar surface as though it were formed in the chromosphere. This allows us to include the X-ray emission by simply adding it to the normal stellar continuum flux (Section 3.2.1). The dependency of the line formation on the different X-ray emission locations is beyond the scope of this paper, but will be explored in the future. In this work, we assume that the X-ray emitting plasma is radiating thermally (as a blackbody) with a single temperature T_X . The thermal X-ray radiation flux is normalised with the total X-ray luminosity L_X (0.1 – 10 keV), which we set as an input parameter. Note that we restrict the contribution of the X-ray emitting gas to the continuum to be only within the X-ray energy range (0.1–10 keV), i.e. the intensity (I_ν) from the X-ray emitting plasma is assumed to be zero for the energy below 0.1 keV and above 10 keV. The attenuation of X-ray flux is not taken into account in our model; however, this is to be improved in a future study. Further discussion on the X-ray optical depth can be found at the end of Section 5.2.

Note that the stellar photospheric continuum in our model (Section 3.2.1) has a relatively low effective temperature (4,000 K); therefore, the stellar flux in EUV (including that at 24.58 eV) is essentially zero. This situation could be also thought as the case when the EUV flux is completely attenuated. With no EUV flux present, the only source of the photoionization of He I in our model is the X-ray emission as described above.

4 MHD MODEL RESULTS

4.1 Input parameters and grid setup

The stellar parameters adopted here are $M_* = 0.8 M_\odot$, $R_* = 2.0 R_\odot$ and $P = 5.38$ d where M_* , R_* and P are the stellar mass, radius and the rotational period, respectively. The corresponding corotation radius and the escape velocity of the system are $6.0 R_*$ and 390 km s^{-1} , respectively. Following, RO09, we set the dimensionless viscosity and diffusivity coefficients (see Section 2.1) to $\alpha_v = 0.3$ and $\alpha_d = 0.1$. For the models presented here, the surface magnetic field strength is fixed at $B_* = 1 \text{ kG}$, and the magnitude of the dipole moment (equation 1) at $\mu = 40$ in the units of B_* . The initial corona temperature is set as $T_c = 9.2 \times 10^6 \text{ K}$, and the disc temperature at the outer boundary is fixed at $T_d = 1.5 \times 10^3 \text{ K}$ (see Section 2.1). The ratio of the corona to disc densities (ρ_c/ρ_c) are fixed at $\sim 1.7 \times 10^{-4}$, and we vary ρ_d to control the disc mass-accretion rate.

The simulations are performed in the radial range, $R_{\text{in}} \leq r \leq R_{\text{out}}$ where $R_{\text{in}} = 1.0 R_*$ and $R_{\text{out}} = 33.7 R_{\text{in}}$, and in the polar angle range, $0 \leq \theta \leq \pi/2$. The grid spacing in θ is uniform, but that in r is chosen such that each side of the curvilinear rectangle cells is approximately equal. The number of grid points used in the models are $n_\theta = 40$ and $n_r = 96$. Note that the grid setup used here is slightly different from those in the conical-shell wind

models of RO09 who used the radial range: $R_{\text{in}} = 2.0 R_*$ and $R_{\text{out}} = 16 R_{\text{in}}$, and the number of grid points: $n_\theta = 31$ and $n_r = 51$. Their corotation radius for a CTTS model is $3.0 R_*$ which is 1/2 of our value. We have run simulations with higher resolutions (e.g. $n_\theta = 80$ and $n_r = 192$), but overall flow patterns as well as the physical quantities (e.g. plasma temperature, density and velocity) are very similar to those of the lower resolution models presented in this work.

4.2 Matter flow in conical-shell winds

We have performed the MHD simulations with ranges of the disc density ρ_d and have examined the dependency of the flows on ρ_d . Here, we present two most representative cases for (1) a relatively high mass-accretion rate (Model A) and (2) a moderate mass-accretion rate (Model B). Fig. 1 shows the maps of density (ρ), poloidal mass-flux ($\Phi_m \equiv \rho v_p$) along with sample magnetic field lines and the directions of the poloidal velocity (v_p), for both models. The main model parameters and the corresponding mass-accretion rates (\dot{M}_a), mass-loss rates in the conical-shell wind (\dot{M}_{cw}) and the mass-loss rates in the polar wind (\dot{M}_{pw}) are summarised in Tab. 1. In the following, each model will be described in more detail.

4.2.1 A relatively high mass-accretion rate case: Model A

This model uses a relatively large disc density (at the outer boundary), $\rho_d = 4.9 \times 10^{-12} \text{ g cm}^{-3}$. The disc matter initially entering from the outer boundary forms an accretion disc around the star, and reaches a semi-steady state as shown in Fig. 1. The high disc density matter pushes the stellar dipole magnetic fields almost all the way to the stellar surface, and a very small funnel ($\sim 1.2 R_*$ in size) is formed. The matter accretes on to the stellar surface through the small funnel with the accretion rate $\dot{M}_a = 3.4 \times 10^{-7} M_\odot \text{ yr}^{-1}$. The geometrically inclined field lines near $r \approx 2 R_*$ on the disc plane and the inflated field above it create conditions favourable for matter from the inner disc region (RO09). The gas flows, from the inner disc region, into a conical-shell shaped wind. The flow is somewhat collimated near the outer boundary and has a half-opening angle $\theta_o \approx 18^\circ$. This is smaller than those of the conical-shell wind simulations of RO09 ($\theta_o \sim 30^\circ - 40^\circ$) who used a smaller radial range ($R_{\text{out}} = 16 R_{\text{in}}$) than our value ($R_{\text{out}} = 33.7 R_{\text{in}}$). On the other hand, Lii et al. (2012) obtained a much more collimated outflow ($\theta_o \approx 4^\circ$) using a larger radial range ($R_{\text{out}} = 42 R_{\text{in}}$).

The poloidal and toroidal velocity components (v_p and v_ϕ) along with the magnitude of the total velocity (v_{tot}) along the conical-shell wind (along the black dashed line in the upper right panel of Fig. 1) are shown in Fig. 2. The rotational speed v_ϕ dominates near the base of the wind, and its value is essentially the same as that of the Keplerian velocity at the wind base. The poloidal component v_p increases along the conical-shell wind, and it peaks around $d \approx 8 R_*$ with $v_p \approx 125 \text{ km s}^{-1}$, then it slowly decreases beyond that point, and v_p reaches $\sim 60 \text{ km s}^{-1}$ when the conical-shell wind escapes from the outer boundary. The slight decrease in v_p at large radii is related to the fact that the reference lines in Fig. 1 are not exactly parallel to the outflow stream lines, and v_p tends to decrease as the distance from the symmetry axis (z) increases at a given value of z . The velocity range found here is consistent with the extent of the narrow blueshifted absorption components (up to $\sim 200 \text{ km s}^{-1}$) in the observed He I $\lambda 10830$ profiles obtained by e.g. ED06.

Table 1. Summary of MHD Models

Model ID	T_d (K)	T_c (K)	ρ_d (g cm^{-3})	ρ_c (g cm^{-3})	\dot{M}_a ($\text{M}_\odot \text{yr}^{-1}$)	\dot{M}_{cw} ($\text{M}_\odot \text{yr}^{-1}$)	\dot{M}_{pw} ($\text{M}_\odot \text{yr}^{-1}$)	Funnel Flow Size (R_*)
A	1.5×10^3	9.2×10^6	4.9×10^{-12}	8.2×10^{-16}	3.4×10^{-7}	8.2×10^{-8}	1.4×10^{-10}	~ 1.2
B	1.5×10^3	9.2×10^6	8.2×10^{-13}	1.4×10^{-16}	4.1×10^{-8}	6.9×10^{-9}	2.6×10^{-10}	~ 2.0

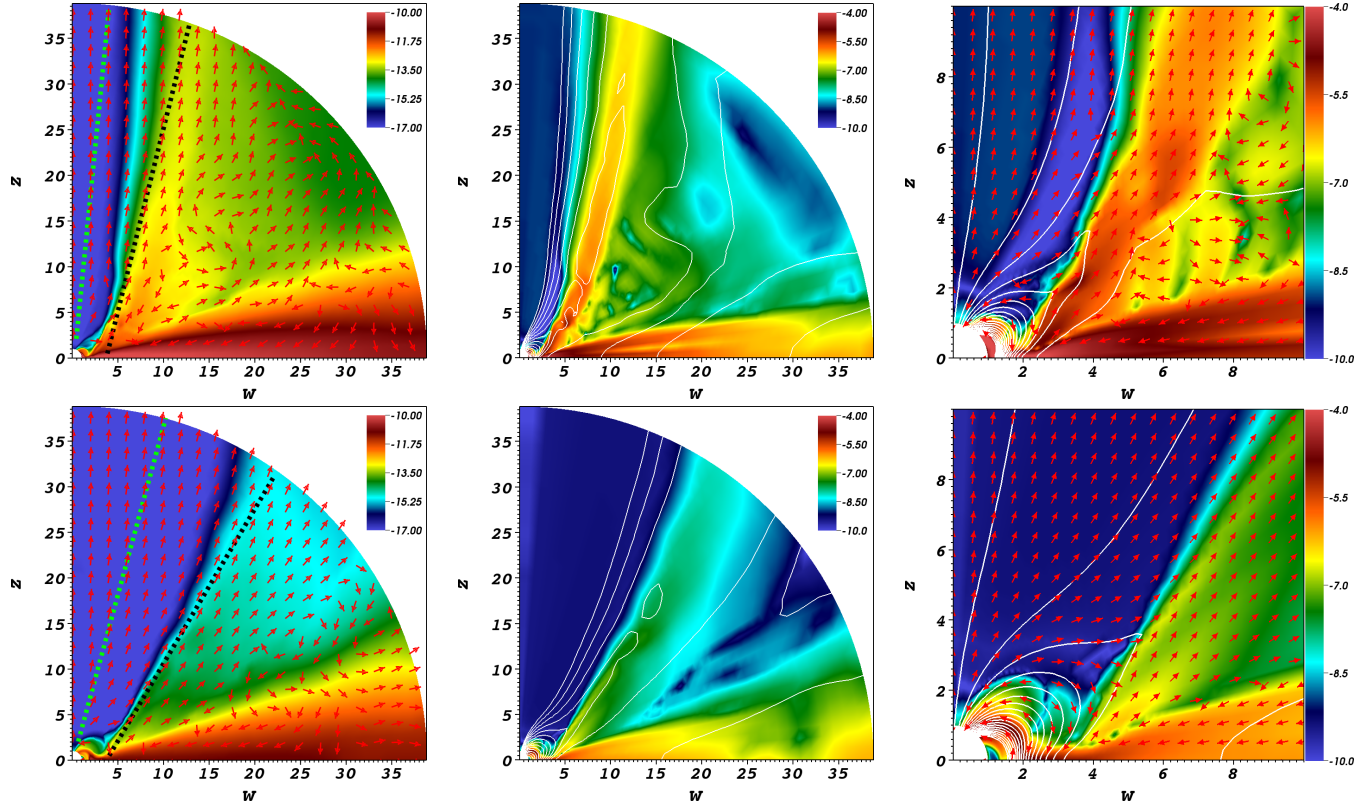


Figure 1. Summary of MHD models with a high mass-accretion rate (Models A; top panels) and a moderate mass-accretion rate (Model B; bottom panels). See Table 1 for the model parameters. The density maps (in logarithmic scale; in cgs units) are over-plotted with the directions of the poloidal velocity (v_p) as arrows (left panels). The poloidal matter flux $v_p \rho$ maps (in logarithmic scale; in cgs units) are shown with sample magnetic field lines (middle panels). The zoom-in poloidal matter flux $v_p \rho$ maps (right panels) are shown with both sample magnetic field lines and poloidal velocity directions as arrows. In the left panels, the reference lines passing through the conical-shell (black dashed line) and polar winds (green dashed line) are also shown. The length scales are in the units of the stellar radius (R_*).

Fig. 1 also shows the lower density and higher speed outflow in the polar direction which we refer to as ‘the polar wind.’ This should be distinguished from ‘the stellar wind’ which arises from/near the stellar surface, but is not implemented in this model. The matter in the polar wind is simply the gas redirected from the upper part of the accretion funnel flow, and it does not originate from the stellar surface. The poloidal component of the velocity in the polar wind (along the green dashed line in the upper right panel of Fig. 1) is also shown in Fig. 2. The polar wind quickly accelerates to about $1.3 \times 10^3 \text{ km s}^{-1}$ in a few stellar radii, and it slowly decelerates beyond $d \approx 15 R_*$. The density in the polar wind is very low and the polar region is magnetically dominated. As a result, the low density gas is accelerated up to a very high velocity via strong magnetic forces. A similar component of the outflow has been observed in the simulations for the propeller regime (a fast stellar rotation regime) (e.g. Ustyugova et al. 2006; Romanova et al. 2009). As mentioned before, the slight decrease in

v_p at large radii seen in Fig. 2 is related to the fact that the reference lines in Fig. 1 are not exactly parallel to the outflow stream lines. This velocity is much larger than the extent of the wide and deep blueshifted absorption feature ($\sim 400 \text{ km s}^{-1}$) in the observed He I $\lambda 10830$ profiles (e.g. ED06). The poloidal velocity of the polar wind is about 10 times larger than that of the conical-shell wind in most of the radial ranges. The mass-loss rates in the conical-shell and polar winds are $\dot{M}_{cw} = 8.2 \times 10^{-8} \text{ M}_\odot \text{yr}^{-1}$ and $\dot{M}_{pw} = 1.4 \times 10^{-10} \text{ M}_\odot \text{yr}^{-1}$, respectively. The former is much larger and the latter is smaller than a typical mass-loss rate of CTTSs ($\sim 10^{-9} \text{ M}_\odot \text{yr}^{-1}$), but they are still within the range of the observed mass-loss rates (e.g. Hartigan et al. 1995).

Although the mass-accretion rate $\dot{M}_a = 3.4 \times 10^{-7} \text{ M}_\odot \text{yr}^{-1}$ found in Model A is much higher than that of a typical CTTS, $\sim 10^{-8} \text{ M}_\odot \text{yr}^{-1}$ (e.g. Gullbring et al. 1998; Hartmann et al. 1998; Calvet, Hartmann, & Strom 2000), it is still an acceptable value for CTTSs (e.g. Hartigan et al. 1995). However, this model is not

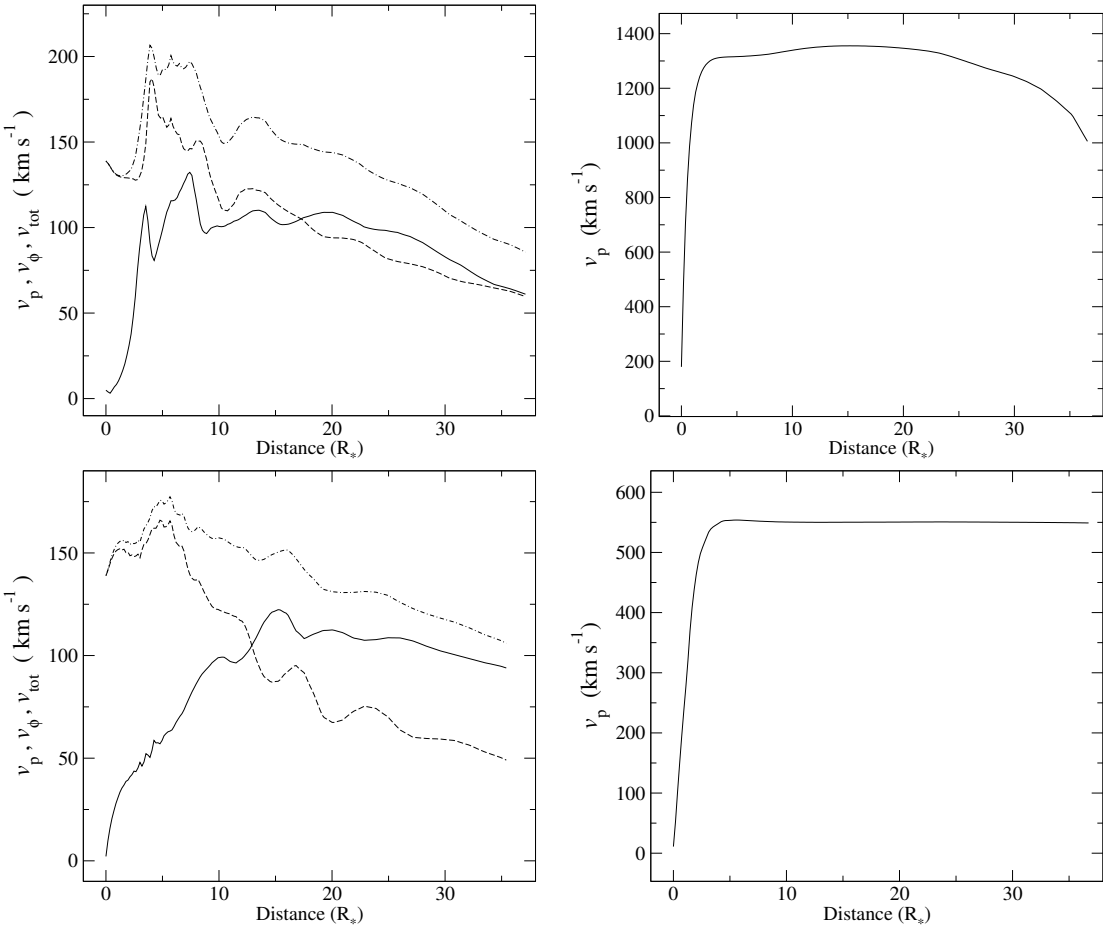


Figure 2. The total speed (v_{tot} ; dash-dot), the poloidal (v_p ; solid) and azimuthal components (v_ϕ ; dash) of the velocity along the reference lines indicated in the left panels of Fig. 1 are shown for Models A (top panels) and B (bottom panels). The horizontal axis indicates the distance (d) from the base of the wind along the reference lines. The panels on the left column are the velocity components along the reference line that goes through the ‘conical-shell winds.’ The panels on the right column show v_p along the reference line that go through ‘the polar wind’. Compared to v_p , v_ϕ is negligibly small and $v_p \approx v_{\text{tot}}$ in the polar wind; hence, they are omitted from the plots.

suitable for modelling line profile for CTTSs because the size of the magnetospheric accretion funnel flow is much smaller than that indicated by previous studies (e.g. Muzerolle, Calvet, & Hartmann 1998a; Muzerolle, Calvet, & Hartmann 2001). The observed line profiles (e.g. Pa β , Br γ and He I $\lambda 10830$) often show redshifted absorption features that often extends to 200–300 km s^{-1} (e.g. Edwards et al. 1994; Alencar & Basri 2000; Folha & Emerson 2001) which are formed in the inflowing gas that is accreting on to the stellar surface through the funnel flows. When the size of the magnetosphere or the funnel flow is too small, the inflow speed in the funnel also becomes too small since the gas gains the kinetic energy from the gravitational potential energy (c.f. Ghosh, Pethick, & Lamb 1977; Hartmann et al. 1994). In Model A, we find that the poloidal velocity of the gas in the funnel flow is only $\sim 120 \text{ km s}^{-1}$ which is much smaller than a typical observed value (200–300 km s^{-1}). Further, the geometry of the funnel flow is not ideal for producing the redshifted absorption feature. Since the funnel flow is located very close to the stellar surface, the funnel stream is almost parallel to the stellar surface. This flow geometry reduces the line-of-sight (recession) speed of the gas toward an observer. The line profile models based on this type of flow will result in a very weak redshifted absorption component with a velocity extent

that is too small when compared to observations. To improve the MHD model to be more suitable for CTTSs, we now attempt to enlarge the size of the accretion funnel by preventing the accretion disc from pushing the stellar dipole magnetic field too close to star.

4.2.2 A moderate mass-accretion rate case: Model B

To reduce the amount of the compression of the magnetosphere towards the stellar surface by the accretion disc, the disc density ρ_d at outer boundary is now reduced by a factor of ~ 6 from the value used in Model A. The lower density plasma reduces the total gravitational force on the magnetic field lines, and consequently the size of the magnetosphere or the accretion funnel becomes much larger ($\sim 2.0 R_*$) than the previous case, Model A. In Model B, the funnel flow is clearly detached from the stellar surface (Fig. 1). The corresponding mass accretion rate on to the stellar surface through the funnel is $\dot{M}_a = 4.1 \times 10^{-8} M_\odot \text{ yr}^{-1}$, which is very similar to the value found for a typical CTTS ($\sim 10^{-8} M_\odot \text{ yr}^{-1}$, e.g. Gullbring et al. 1998; Hartmann et al. 1998; Calvet et al. 2000), and is about ~ 8 times smaller than that of Model A. The inner edge of the accretion disc is now located $\sim 2.0 R_*$ from the origin, and the outflow in the conical-shell wind originates at a larger distance

$r \approx 4.0 R_*$ (in the disc plane) which is slightly smaller than the corotation radius ($R_{\text{cr}} = 6.0 R_*$).

The outflow geometry is similar to that of Model A, but the wind is less collimated with its half-opening angle of the conical-shell wind (measured at the outer boundary) $\theta_o \approx 35^\circ$ (Fig. 1), which is similar to the value found in RO09. Fig. 2 also shows the poloidal and toroidal velocity components (v_p and v_ϕ), and the magnitude of the total velocity (v_{tot}) along the conical-shell wind (along the black dashed line in the lower right panel of Fig. 1). As also seen in Model A, the rotational speed v_ϕ dominates near the base of the wind. The poloidal component v_p increases along the conical-shell wind, and it peaks around $d \approx 15 R_\odot$ with $v_p \approx 125 \text{ km s}^{-1}$. The flow then slowly decelerates beyond that point, and v_p reaches $\sim 90 \text{ km s}^{-1}$ near the outer boundary. As in the previous model (Model A), the slight decrease in v_p at large radii is related to the fact that the reference lines in Fig. 1 are not exactly parallel to the outflow stream lines.

Again, this velocity range in the conical-shell wind is consistent with the velocity range of the narrow blueshifted absorption components (up to $\sim 200 \text{ km s}^{-1}$) found in the observed He I $\lambda 10830$ profiles (e.g. ED06). Note that the outflow speed (v_p) in the conical-shell wind in Model B is similar to that of Model A. The polar wind quickly accelerates to $\sim 550 \text{ km s}^{-1}$ (along the green dashed line in the lower right panel of Fig. 1) at the distance $d \approx 5 R_*$ from the base of the wind. The wind speed then slightly decreases, but it remains almost constant all the way to the outer boundary. The outflow speed (v_p) of the polar wind in Model B is about 2 times less than that of Model A. This velocity is comparable to the extent of the wide and deep blueshifted absorption feature ($\sim 400 \text{ km s}^{-1}$) in the observed He I $\lambda 10830$ profiles (e.g. ED06). The mass-loss rates in the conical-shell and polar winds are $\dot{M}_{\text{cw}} = 6.9 \times 10^{-9} M_\odot \text{ yr}^{-1}$ and $\dot{M}_{\text{pw}} = 2.6 \times 10^{-10} M_\odot \text{ yr}^{-1}$, respectively. The former is larger and the latter is smaller than a typical mass-loss rate of CTTSs ($\sim 10^{-9} M_\odot \text{ yr}^{-1}$), but they are still within the range of the observed mass-loss rates (e.g. Hartigan et al. 1995).

The geometry of the well defined accretion funnel in Model B is very similar to that of the magnetospheric accretion funnels used in hydrogen line profiles models e.g. Hartmann et al. (1994), Muzerolle et al. (2001), Symington, Harries, & Kurosawa (2005a) and Kurosawa et al. (2006) who adopted the axisymmetric magnetosphere model of Ghosh et al. (1977) (see also Ghosh & Lamb 1979a; Ghosh & Lamb 1979b). These models have been successfully demonstrated that the redshifted absorption features or the inverse P-Cygni profiles seen in some of the observed hydrogen lines can be explained by the absorption by the inflowing gas through the magnetospheric accretion funnels. In Model B, we find that the flow speed in the funnel near the stellar surface reaches $\sim 250 \text{ km s}^{-1}$, which is very similar to the values seen in the observation, 200–300 km s^{-1} (e.g. Edwards et al. 1994; Muzerolle, Hartmann, & Calvet 1998b; Alencar & Basri 2000; Folha & Emerson 2001).

In summary, Model B shows very similar inflow and outflow velocities, mass-loss and mass-accretion rates to those found in the observations. Hence, it is a very good candidate for being tested with our radiative transfer model which uses the MHD simulation results as model inputs. In the following, we describe the hydrogen and helium line profile models based on the flow solution found in Model B.

Table 2. Summary of line profile model parameters

Model ID	T_{max} (10^3 K)	L_X ($10^{30} \text{ erg s}^{-1}$)	T_X (10^6 K)	γ_{He^1} (10^{-4} s^{-1})
B1	8	4	2	1.2
B2	10	4	2	1.2
B3	14	4	2	1.2
B4	10	0.4	2	0.12
B5	10	20	2	6.0
B6	10	4	5	0.2
B7	10	4	20	0.012

5 LINE PROFILE MODELS

We now investigate whether the MHD outflows found in Model B of the previous section is a plausible solution for CTTSs, by computing line profiles based on the simulation, and by checking the consistency with the existing spectroscopic observations. The stellar parameters adopted here are same as in Section 4.1, and the continuum sources as described in Section 3.2. The density, velocity and temperature (but see Section 5.1) found in Model B are mapped on to the radiative transfer grid (e.g. KU11), and used as input variables in the profile calculation. We exclude the high density disc accretion disc region (indicated by the dashed line in Fig. 3), and concentrate on modelling the line emission and absorption only from the accretion funnel and the outflow regions. The disc region is excluded from the computations because of the gas temperature near the inner part of the disc, especially near the inner edge of the disc, is too high ($T \sim 10^5 \text{ K}$) in the simulation result from Model B (Fig. 3). If the relatively high temperature gas near the inner edge of the disc is included, the line emission is dominated from this region, and the line strengths are unrealistically strong. The disc temperature at larger radii ($r > 20 R_*$) are low 1,500–2,000 K, and we do not expect any significant contribution to the atomic hydrogen and helium emission. To mimic the opaqueness of the accretion disc, we simply place a geometrically thin but optically thick disc on the equatorial plane with the inner radius corresponding to the inner radius of the high density MHD disc region (the vertical dashed line in Fig. 3) which is removed from the radiative transfer calculation.

In the following, we examine the dependency of the line profiles on our main model parameters: the maximum gas temperature (T_{max}), X-ray luminosity (L_X) and the temperature of the X-ray emitting gas (T_X) (cf. Section 3.2.3). The model parameters are summarised in Table 2. To examine the dependency of the line profiles on the model parameters, we mainly focus on modelling the lines which often show a sign of wind (a blueshifted absorption component), namely H α and He I $\lambda 10830$. In the following two sections (Sections 5.1 and 5.2), example line profiles are calculated at $i = 30^\circ$ because He I $\lambda 10830$ profile exhibits both the blueshifted wind absorption and the redshifted magnetospheric absorption most clearly at this inclination angle. However, readers should be aware that the probabilities of observing an object with $i < 30^\circ$ and $i > 30^\circ$ are 0.134 and 0.866, respectively. Example calculations of additional hydrogen and helium lines, and their dependency on the inclination angle (i) will be also presented in Section 5.3.

5.1 Dependency on the maximum gas temperature

Our initial calculations of the line profiles based on the MHD simulation Model B, with unmodified temperature structure from the

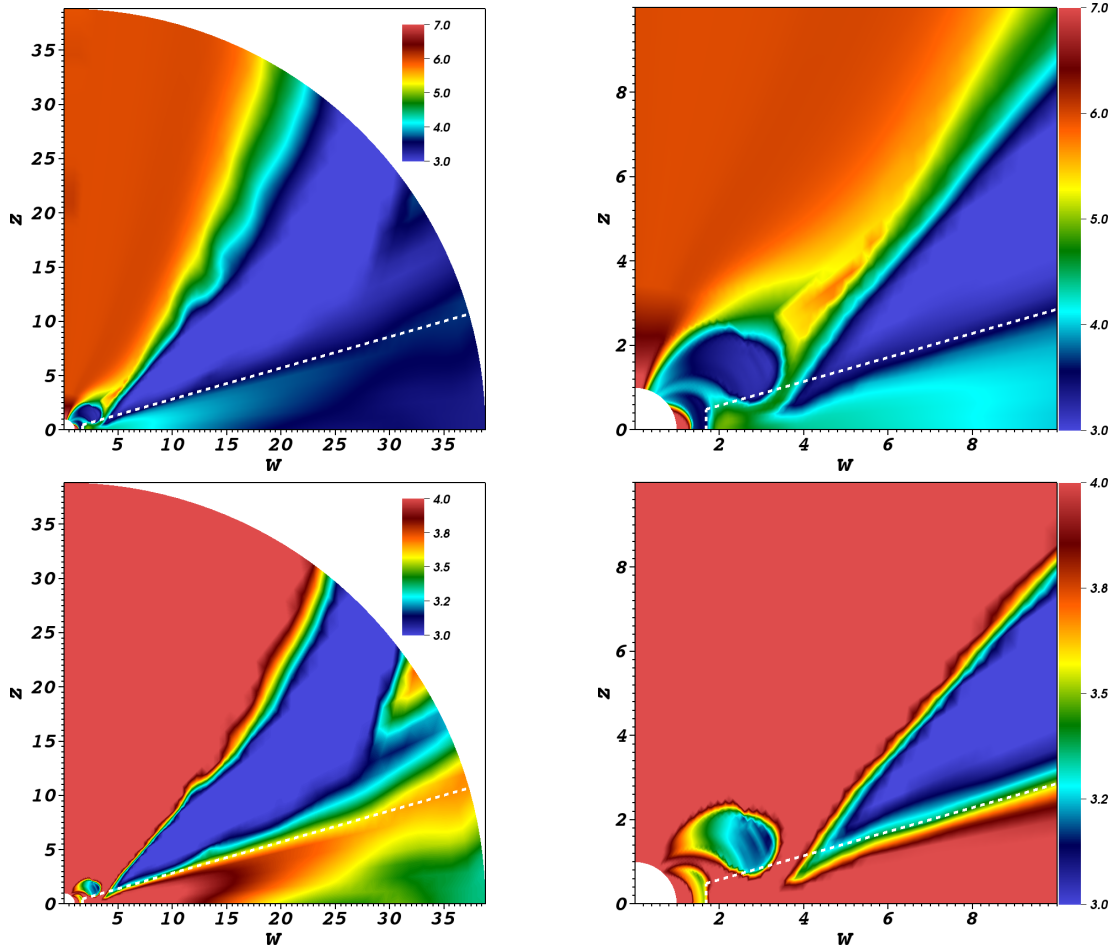


Figure 3. The temperature maps (in logarithmic scale; in K) of MHD Model B (cf. Table 1 and Fig. 1) in full-scale (*left panels*) and in small-scale (*right panels*). The *upper panels* show the original temperatures (unmodified) from the MHD simulation. The *lower panels* show the temperatures from the same MHD simulation, but the upper limit of the temperature is set to $T_{\max} = 10^4$ K. N.B. the different temperature ranges are used in the colour indeces for the upper and lower panels. The temperature maps from the lower panels are adopted in the line profile calculation (see Section 5.1). The high density disc zone, indicate by the *dashed lines* is excluded from our line profile calculations. See Section 5.1 for explanations. The length scales are in the units of the stellar radius (R_*).

simulations, showed that the line strengths (e.g. H α) are unrealistically too strong when compared with observations (e.g. Reipurth et al. 1996). This is mainly due to the emission from the relatively high temperature gas ($\sim 10^5$ K) near the interface between the relatively high density conical-shell wind region and the low density polar wind region (Fig. 3). The original temperature of the flows in the outflows are, in general, higher than the typical wind temperatures used in our previous line profile models ($\sim 10^4$ K, KU11) which showed reasonable agreement with the observed CTTSs. A recent local excitation study for line opacities of CTTSs by Kwan & Fischer (2011) has also found a similar temperature range. When the gas from the inner part of the disc is ejected to the wind, it cools down due to the adiabatic expansion, which is treated properly in the MHD simulations. However, the additional radiative cooling mechanism, which is not included in the simulation, may be required to cool down the gas even further. In general, the temperatures from the MHD simulations could be quite uncertain. We therefore modify the original gas temperature of the MHD simulations, in order to match observed line profiles, and treat the temperature as though a free parameter in the line profile calculations. For this reason, we limit the maximum temperature (T_{\max}) of the

gas from the MHD simulation to be $\sim 10^4$ K when it is applied to the radiative transfer models.

The lower panels in Fig. 3 show the temperature maps of MHD Model B when the maximum allowed temperature $T_{\max} = 10^4$ K is applied. The figures show that T_{\max} not only affects the low density and high temperature polar wind regions, but also affect the conical-shell wind region. The relatively high density conical-shell wind region (including its base), is essentially isothermal (with $T = T_{\max} = 10^4$ K) in this case. On the other hand, the original temperature of the accretion funnel from the MHD simulation (the upper panels in Fig. 3), is relatively low compared to the wind temperature and is mostly less than $\sim 10^4$ K. However, the temperatures in the funnel flow near the stellar surface and near the accretion disk are slightly higher than 10^4 K (in the original temperature from the MHD simulation); hence, they are affected by the imposition of T_{\max} . In the following, we examine the effect of changing T_{\max} on the computed line profiles.

Fig. 6 shows the model line profiles for H α and He I $\lambda 10830$ computed for $T_{\max} = 8.0 \times 10^3$, 1.0×10^4 and 1.4×10^4 K (Models B1, B2 and B3 in Table 2). The inclination angle, the X-ray luminosity and temperature are fixed at $i = 30^\circ$, $L_X =$

4×10^{30} erg s $^{-1}$ and $T_X = 2 \times 10^6$ K, respectively. The strengths of the emission lines are comparable to those found in observations (e.g. Reipurth et al. 1996; Edwards et al. 1994; Muzerolle et al. 1998b; Alencar & Basri 2000; ED06) in this temperature range.

The line profile morphology of the He I $\lambda 10830$ models are also similar to some of the observed line profiles found in ED06. In particular, they are similar to those which exhibit a narrow blueshifted absorption component that often extends to ~ 200 km s $^{-1}$. The relatively narrow blueshifted absorption components, centred around $v \approx -120$ km s $^{-1}$, seen in the models are caused by the outflowing gas in the conical-shell wind, and the redshifted absorption component, which shows the minimum flux at $v \sim 100$ km s $^{-1}$ and extends to $v \sim 250$ km s $^{-1}$ is caused by the inflowing gas that is accreting onto the stellar surface through the accreting funnel. The figure shows that the emission strength and the absorption components (in both red and blue wing) of He I $\lambda 10830$ are rather insensitive to the gas temperatures in this range. This is because of the relatively large ionization potential (24.6 eV) of He I, and the plasma temperature is not quite high enough for significant collisional excitations. The main cause of the excitation for He I in these models are due to photoionizations e.g. by the X-ray flux (c.f. KU11).

On the other hand, the emission strengths of the model H α is sensitive to T_{\max} value. The line emission becomes stronger as T_{\max} increases. Relatively weak but clearly visible absorption components are seen in the blue wing of the line ($v \approx -120$ km s $^{-1}$). This, again, is caused by outflowing in the conical-shell wind. Unlike He I $\lambda 10830$, the redshifted absorption component that goes below the continuum level is absent from the H α profiles. This is consistent with observations (e.g. Reipurth et al. 1996) which find that H α profiles of CTTSs rarely show redshifted absorption below the continuum. For $T_{\max} = 1.4 \times 10^4$ K, the line centre flux reaches ~ 30 (normalised to the continuum) which is close to the maximum value found in the observations. The peak flux of the H α profiles computed with $T_{\max} = 1.0 \times 10^4$ K is ~ 15 (normalised to the continuum) which is similar to typical values found in observations. In summary, based on the line strengths of H α in Fig. 4 in comparison with those of typically observed H α , the gas temperature of the accretion funnel and the conical-shell wind in this particular MHD simulation should be less than $\sim 1.4 \times 10^4$ K. In the rest of this paper, we adopt $T_{\max} = 1.0 \times 10^4$ K in our line profile calculations.

Here, we have adopted a rather simplistic method of the gas temperature assignment, with the introduction of T_{\max} parameter. However, this leads to a large reduction of temperatures (from $\sim 10^6$ K to $\sim 10^4$ K) in the low-density polar wind region where the gas temperature may be less affected by the radiative cooling. The limiting the gas temperature to $\sim 10^4$ K in the polar wind region would be reasonable when the wind density there is very low; hence, the omission of the opacity in the polar wind region does not affect the line profiles. On the other hand, if the polar wind density becomes relatively high, the wind opacity may become high enough to affect the line profile; therefore, the temperature of the polar wind should be treated more properly.

5.2 Dependency on X-ray luminosity and temperature

Next, we examine the dependency of the model profiles on the X-ray luminosity (L_X) and the temperature of the X-ray emitting gas (T_X). As in Section 3.2.3, our models assume that the X-ray emitting plasma is radiating thermally (as a blackbody) with a single temperature T_X . The thermal X-ray radiation flux is normalised

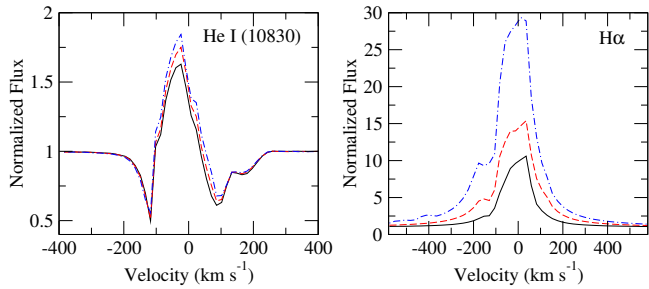


Figure 4. Dependency of He I $\lambda 10830$ (left) and H α (right) on the maximum gas temperature allowed (T_{\max}) in the profile calculations. MHD Model B is used for all the models shown here. The profiles are computed at the fixed inclination angle $i = 30^\circ$ and fixed X-ray luminosity and temperature, which are $L_X = 4 \times 10^{30}$ erg s $^{-1}$ and $T_X = 2 \times 10^6$ K, respectively. The models shown here use $T_{\max} = 8.0 \times 10^3$ (solid), 1.0×10^4 (dash), and 1.4×10^4 K (dash-dot), which corresponds to Models B1, B2 and B3 in Table 2, respectively.

with the total X-ray luminosity L_X (0.1 – 10 keV). The photoionization process by high energy photons are expected to be important for the formation of the wind sensitive line, He I $\lambda 10830$ (c.f. Kwan & Fischer 2011; KU11).

Fig. 5 shows the model He I $\lambda 10830$ profiles computed for $L_X = 4 \times 10^{29}$, 4×10^{30} and 2×10^{31} erg s $^{-1}$ (Models B4, B2 and B5 in Table 2), which are within the range of observed values for CTTSs (e.g. Telleschi et al. 2007; Güdel & Telleschi 2007; Güdel M. et al. 2010). The inclination angle and the X-ray temperature are fixed at $i = 30^\circ$ and $T_X = 2 \times 10^6$ K, respectively. The corresponding photoionization rates of He I from the ground state (γ_{HeI}) at a typical location in the wind ($r = 5.6R_*$) for Models B4, B2 and B5 are 1.2×10^{-5} , 1.2×10^{-4} and 6.0×10^{-4} s $^{-1}$, respectively (Table 2). Since the X-ray flux is directly proportional to a value of L_X , the photoionization rate γ_{HeI} is also proportional to L_X (see Table 2). The photoionization rates here are similar to those found in Kwan & Fischer (2011), i.e. $\gamma_{HeI} \approx 10^{-5} - 10^{-4}$ s $^{-1}$ in the local excitation calculation of the plasma, in the context of the classical T Tauri stellar wind.

The X-ray luminosity between 4×10^{29} and 2×10^{31} erg s $^{-1}$ (or equivalently γ_{HeI} between 1.2×10^{-5} and 6.0×10^{-4} s $^{-1}$) produces resonable line strengths in He I $\lambda 10830$ when compared to observations (e.g. ED06), and the line is very sensitive to this parameter. As in the previous tests for T_{\max} (Fig. 4), the model He I $\lambda 10830$ profiles show both the redshifted absorption caused by the accretion funnel and the blueshifted absorption component caused by the conical-shell wind. The figure shows that the line centre flux becomes larger as L_X (or equivalently γ_{HeI}) increases. Similarly, the depths of the absorption components on the blue sides become deeper and wider as the value of L_X (or equivalently γ_{HeI}) increases. Interestingly, for the model with the largest L_X (2×10^{31} erg s $^{-1}$), the blue absorption component extends to ~ -200 km s $^{-1}$ which is larger than a typical maximum speed observed in the conical-shell wind (see Fig. 2). Although the deepest and main part of the blueshifted absorption (~ -120 km s $^{-1}$) is caused by the relatively high density conical-shell wind, the shallower but higher velocity absorption is caused by the lower density and higher velocity (Fig. 2) gas in the polar wind. For the largest L_X model, there are enough high energy photons to photoionize He I in the polar wind, and the He I $\lambda 10830$ opacity in the polar wind becomes non-negligible.

The figure also shows the model H α profiles computed for the

same set of L_X values. Unlike He I $\lambda 10830$, H α is insensitive to the value of L_X , and the computed profiles for all three L_X values are almost identical to each other. The model H α profile does not depend on the value of L_X mainly because the photoionization rates for ‘H I’ in the X-ray energy range (0.1 – 10 keV) used here is small compared to the collisional rates in the relatively high density gas in the funnel flow. A weak blueshifted absorption component, caused by the conical-shell wind, is also seen at $v \sim -120 \text{ km s}^{-1}$. Unlike the blueshifted absorption component seen in the He I $\lambda 10830$ model with the largest L_X , the wind absorption here does not extend to a high velocity (e.g. $\sim -200 \text{ km s}^{-1}$); hence, the polar wind is not contributing to the absorption in the H α model profiles here.

We now examine the effect of changing the X-ray temperature T_X on the profiles. Fig. 6 shows the model He I $\lambda 10830$ profiles computed for $T_X = 2 \times 10^6$, 5×10^6 and 2×10^7 K (Models B2, B6 and B7, respectively in Table 1). The inclination angle and the X-ray luminosity are fixed at $i = 30^\circ$ and $L_X = 4 \times 10^{30} \text{ erg s}^{-1}$ for all three models. The corresponding photoionization rates of He I ($\gamma_{\text{He I}}$) at a typical location in the wind ($r = 5.6 R_*$) for Models B2, B6 and B7 are 1.2×10^{-4} , 2.0×10^{-5} and $1.2 \times 10^{-6} \text{ s}^{-1}$, respectively (see Table 2). For a fixed L_X value and in this temperature range, the photoionization rate of He I ($\gamma_{\text{He I}}$) decreases as T_X increases because the peak of the blackbody radiation curve shifts to a higher wavelength. Since the X-ray flux is normalized to a fixed value of L_X , this leads to a reduction of the softer X-ray flux when T_X is increased. Consequently, the photoionization rate of He I decreases because its photoionization cross section is much larger towards the EUV frequency.

The line strengths of the model He I $\lambda 10830$ profiles computed with this range of T_X are comparable similar to those found in the observations (e.g. ED06). The line is sensitive to the change in the value of T_X (or equivalently $\gamma_{\text{He I}}$). The flux at the line centre decreases as T_X increases (or equivalently as $\gamma_{\text{He I}}$ decreases), and both blueshifted and redshifted absorption components becomes weaker as T_X increases (or equivalently $\gamma_{\text{He I}}$ decreases). Similar to the earlier cases (Fig. 5), the model H α profiles are not sensitive to the change in T_X value, i.e. the model profiles are almost identical to each other. Again, the line is insensitive to the change in T_X or more precisely to change in the X-ray flux because the photoionization rates for H I in the X-ray energy range (0.1 – 10 keV) is small compared to the collisional rates.

As mentioned earlier (Section 3.2.3), the attenuation of the X-ray flux is neglected in our level population calculations; hence, it is implicitly assumed that the X-ray radiation is optically thin. To check the validity of this assumption, we have calculated the X-ray optical depth (τ_X) at the photon energies $h\nu = 0.1, 1.0$ and 10.0 keV along the line of sight to an observer located at the inclination $i = 60^\circ$. We found $\tau_X \approx 90, 0.4$ and 0.01 for $h\nu = 0.1, 1.0$ and 10.0 keV , respectively. This suggests that the X-ray flux should be almost completely attenuated for all photons with $h\nu < 1.0 \text{ keV}$. On the other hand, the X-ray flux at $h\nu > 1.0 \text{ keV}$ are unaffected by the X-ray opacity.

To assess the effect of the X-ray attenuation on the model profiles, we do the following: (1) compute the continuum optical depth τ_X at all frequency in X-ray, (2) attenuate the X-ray flux by a factor of $e^{-\tau_X}$ at each X-ray frequency, (3) recompute line profiles (including source function calculations) using the X-ray flux corrected for the attenuation due to X-ray opacity, and (4) compare the new line profiles with the models computed without the attenuation of the X-ray flux. For this test, we use He I $\lambda 10830$ line only since H α profiles are rather unaffected by the X-ray flux as previ-

ously seen in Figs. 5 and 6. We have recomputed the He I $\lambda 10830$ line profiles for Models B2 and B6 (Table 2) with the X-ray flux with the attenuation. Note that these two models have the X-ray luminosity $L_X = 4 \times 10^{30} \text{ erg s}^{-1}$ but have different X-ray temperatures, $T_X = 2 \times 10^6$ and 5×10^6 K, respectively. The results are shown in Fig. 7.

The figure shows that the reduction of the line emission and absorption strengths due to the attenuation of the X-ray flux is significant, for a relatively low X-ray temperature (Model B2: $T_X = 2 \times 10^6$ K). However, the effect of the X-ray attenuation becomes notably smaller for the model with a higher X-ray temperature (Model B6: $T_X = 5 \times 10^6$ K). The difference is mainly caused by the difference in the flux distributions of the blackbody radiation curve for different X-ray temperatures. The X-ray flux of the lower X-ray temperature ($T_X = 2 \times 10^6$ K) peaks at a lower energy ($h\nu \approx 0.5 \text{ keV}$) than that of the higher temperature ($T_X = 5 \times 10^6$ K) which peaks at $h\nu \approx 1.2 \text{ keV}$. As mentioned earlier, the X-ray attenuation is important mostly for the photon energies $h\nu < 1.0 \text{ keV}$. This indicates that a larger fraction of X-ray flux is affected/attenuated for the blackbody radiation curve with the smaller temperature ($T_X = 2 \times 10^6$ K) since its peak is located below 1.0 keV. Consequently, the photoionization rate of He I is less affected for the higher T_X model (Model B6); hence, the line profile for He I $\lambda 10830$ is less affected for the higher T_X .

From this test, it is clear that the assumption of no X-ray attenuation could significantly overestimate the line emission and absorption strengths in He I $\lambda 10830$. In this test, we have considered the models with the X-ray flux attenuation which is calculated from the opacity of the models with no X-ray attenuation; hence, they are not completely self-consistent. This method may be acceptable for obtaining rough estimates of the effect of the X-ray attenuation on the line profiles. However, to implement the X-ray attenuation effect properly in our radiative transfer model (KU11), the radiation field (including the X-ray radiation) and opacity must be solved simultaneously. This requires an iteration between the opacity and the radiation field calculations until they are mutually consistent. Unfortunately, our radiative transfer code (KU11) is not designed for this type of iterations, and we have to assume that the gas is optically thin for the underlying continuum source. This is a limitation of our radiative transfer model and is an important caveat. Therefore, we warn readers that the emission and absorption strengths of He I lines presented in this work could be overestimated significantly due to the assumption of no X-ray attenuation in our model.

However, in reality, the magnetospheric accretion funnel, which is a significant contributor to the X-ray optical depth, may not be axisymmetric, and it could occur in two or more funnel streams, as shown in 3D MHD simulations (e.g. Romanova et al. 2003). This flow geometry may contain large gaps between the funnel flows, and it could allow a large fraction of the X-ray produced near the stellar surface to reach the conical-shell regions without a significant attenuation, and ionize He I in the wind.

5.3 Dependency on inclination angle and additional lines

We now examine the dependency of the model profiles on the inclination angles (i) and study the general characteristics by using the set of model parameters used for Model B2 (see Table 2), i.e. $T_{\text{max}} = 1.0 \times 10^4 \text{ K}$, $L_X = 4 \times 10^{30} \text{ erg s}^{-1}$ and $T_X = 2 \times 10^6 \text{ K}$. In addition to He I $\lambda 10830$ and H α , samples of He I $\lambda 5876$, H β , Pa β and Pa γ line profiles are also computed. Since the accretion disc region ($\theta \gtrsim 65^\circ$ as shown in Fig. 3) is excluded in the opacity and emissivity calculations, the line pro-

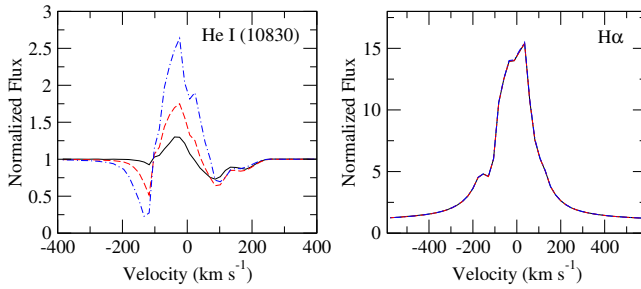


Figure 5. Dependency of He I $\lambda 10830$ and H α profiles on the X-ray luminosity L_X . The MHD simulation, Model B, is used for all the models shown here. The profiles are computed at the fixed inclination angle $i = 30^\circ$ and fixed X-ray emitting plasma temperature $T_X = 2 \times 10^6$ K (assumed isothermal). The values of L_X used are 4×10^{29} (solid), 4×10^{30} (dashed) and 4×10^{31} erg s $^{-1}$ (dash-dot), which corresponds to Models B4, B2 and B5 in Table 2, respectively. The X-ray luminosity between 4×10^{29} and 4×10^{31} erg s $^{-1}$ produces reasonable line strengths in He I $\lambda 10830$ when compared to observations (e.g. ED06). The model H α profiles are not affected by the change in the values of L_X , i.e. three line profiles are almost identical to each other.

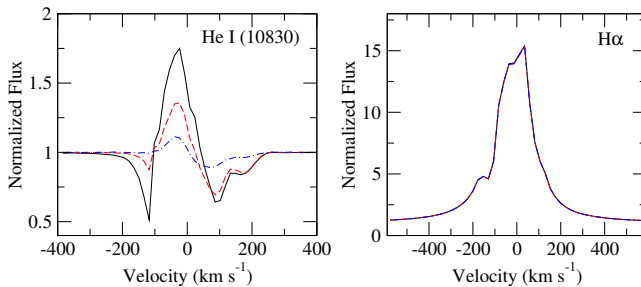


Figure 6. Dependency of He I $\lambda 10830$ and H α profiles on the X-ray temperature T_X . The MHD simulation, Model B, is used for all the models shown here. The profiles are computed at the fixed inclination angle $i = 30^\circ$ and with the fixed X-ray luminosity $L_X = 4 \times 10^{30}$ erg s $^{-1}$. The values of T_X used are 2×10^6 (solid), 5×10^6 (dashed) and 2×10^7 K (dash-dot), which corresponds to Models B2, B6 and B7 in Table 2, respectively. The X-ray temperature between 2×10^6 and 2×10^7 erg s $^{-1}$ produces reasonable line strengths in He I $\lambda 10830$ when compared to observations (e.g. ED06). The model H α profiles are not affected by the change in the values of T_X , i.e. three line profiles are almost identical to each other.

files presented hereafter are restricted to $i < 65^\circ$. This is done also to avoid the complication that arises from the occultation of the line emission by the extended disc which we do not treat self-consistently. We choose four different inclination angles, equally spaced in $\cos i$ between $i = 0^\circ$ and 65° , to present the profiles of equal probability of occurrence between the inclination angle range, i.e. they are approximately $i = 22^\circ, 38^\circ, 50^\circ$ and 60° . The results are summarized in Fig. 8. In general, the line strengths of the model profiles are comparable to those found in observations (e.g. Reipurth et al. 1996; Edwards et al. 1994; Muzerolle et al. 1998b; Alencar & Basri 2000; Folha & Emerson 2001; ED06), except for He I $\lambda 5876$ which are much weaker than a typical value from observations (see e.g. Beristain, Edwards, & Kwan 2001). In the following, the characteristics of each line are examined more closely.

He I $\lambda 10830$. The conical-shell wind geometry with the half-opening angle $\sim 35^\circ$ (Section 4.2.2) does not favour the wind absorption at a low inclination (e.g. $i = 22^\circ$). The blueshifted

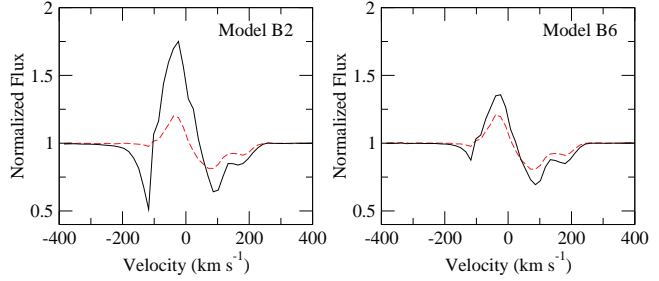


Figure 7. Demonstration of the effect of the X-ray opacity on the formation of He I $\lambda 10830$. The He I $\lambda 10830$ line profiles from Models B2 ($T_X = 2 \times 10^6$ K) and B6 ($T_X = 5 \times 10^6$ K) (solid) are compared with the same models computed with the input X-ray continuum fluxes corrected for the attenuation by the continuum optical depth in X-ray (dash). Note that the original Models B2 and B6 have the same X-ray luminosity, $L_X = 4 \times 10^{30}$ erg s $^{-1}$ (Table 2). For a relatively low X-ray temperature ($T_X = 2 \times 10^6$ K) (left panel), the reduction of the line emission and absorption strengths due to the attenuation of the X-ray flux is significant. The effect of the X-ray attenuation becomes smaller for the model with a higher X-ray temperature ($T_X = 5 \times 10^6$ K) (right panel).

absorption, caused by the conical-shell wind, starts to appear at $i \approx 30^\circ$. The position of the blueshifted absorption shifts from $v \sim 120$ km s $^{-1}$ (at $i \approx 38^\circ$) towards the line centre as the inclination becomes higher (up to $i \approx 60^\circ$). This shift is caused by the change in the line-of-sight velocity of the conical-shell wind toward the observer as the inclination changes. The redshifted absorption, caused by the accretion funnel (c.f. Fig. 1), is present for all i . The extent of the redshifted absorption changes between ~ 200 to ~ 250 km s $^{-1}$ depending on i , which is similar to the flow speed of the gas in the accretion funnel near the stellar surface (c.f. Section 4.2.2). At higher inclination angles ($i \gtrsim 50^\circ$), the line emission almost disappears, and the profile is shaped by the wind and funnel absorption features.

He I $\lambda 5876$. The line peak flux slightly decreases and the redshifted absorption component becomes stronger as the inclination increases. No blueshifted wind absorption component is seen in this line for all i . This is in agreement with the observation of Beristain et al. (2001). The redshifted absorption components, on the other hand, are present for all i . However, the observations of this line, from 31 CTTSs (Beristain et al. 2001), show that the redshifted absorption is rather rare (3 out 31). The line peak fluxes in our models are between ~ 1.1 and ~ 1.2 (normalised to continuum) which are much smaller than those found in the observations (typically > 1.2 , e.g. Alencar & Basri 2000; Beristain et al. 2001). This line is thought to arise from the post shock region of the accretion funnel near the stellar surface (e.g. Beristain et al. 2001; Edwards et al. 2003; Orlando et al. 2010; Kwan & Fischer 2011). This indicates that a higher temperature and density gas may be needed in order to match the observations which would require more formal treatment of the shock regions in the accretion funnels (e.g. Lamzin 1998; Koldoba et al. 2008; Sacco et al. 2008; Orlando et al. 2010).

H α . Unlike the helium lines, no clear redshifted absorption component is seen in this line. However, the profile at the low inclination ($i = 22^\circ$) shows a slight blue asymmetry, i.e. the flux distribution is slightly shifted toward blue, which may be caused by a small amount of absorption in the red wing although it is not seen as a discrete absorption component. At a low inclination angle ($i \approx 22^\circ$), no clear blueshifted wind absorption component is seen in the model profiles. A wind absorption becomes visible for $i \gtrsim 38^\circ$, and its strength increases as i increases. In general,

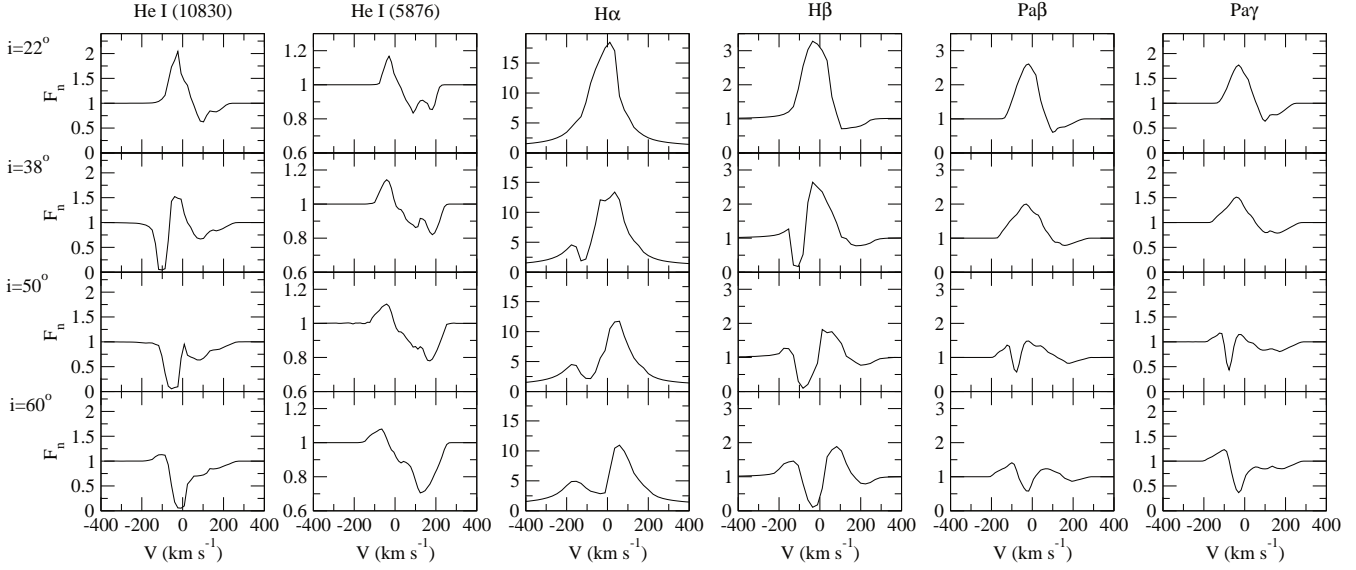


Figure 8. Summary of sample model hydrogen and helium line profiles computed at four different inclination angles: $i = 22^\circ, 38^\circ, 50^\circ$ and 60° (equally spaced in $\cos i$ between $i = 0^\circ$ and 65°) from the top to bottom rows, respectively. From the left to right columns, sets of He I $\lambda 10830$, He I $\lambda 5876$, H α , H β , Pa β and Pa γ profiles are shown respectively. The X-ray luminosity $L_X = 4 \times 10^{30}$ erg s $^{-1}$ and temperature $T_X = 2 \times 10^6$ K (Model B2 in Table 2) are used for all the models shown here. The fluxes (F_n) are normalised to the local continuum.

the models are in good agreement with observations (e.g. Reipurth et al. 1996; Edwards et al. 1994; Muzerolle et al. 1998b; Alencar & Basri 2000). The model profiles here belong to Type I and Type III B (which constitute about 60 per cent of the observed H α profiles for CTTSSs in Reipurth et al. 1996) according to the morphological classification of Reipurth et al. (1996).

H β . The redshifted absorption component is present in the profiles at all i . The extent of the redshift absorption changes between ~ 200 to ~ 250 km s $^{-1}$ depending on i . While no blueshifted absorption component is seen at the lower inclination angles (e.g. $i = 22^\circ$), a strong blueshifted wind absorption component is present at higher inclinations ($i > 38^\circ$). The position of the wind absorption component shifts toward the line centre as i further increases. At $i = 60^\circ$, the wind absorption component is located near $v = 0$ km s $^{-1}$, and the resulting line has a double peaked profile shape. At a very high inclination angle, the conical-shell wind is moving almost perpendicular to the line of sight to an observer; hence, the wind absorption is located near the line centre. The double-peak profile resembles that from a rotating disc; however, the H β emission here mainly arises from the magnetospheric accretion funnel whose rotational velocity is rather slow (~ 20 km s $^{-1}$). The extent of the emission in the blue wing becomes larger as i increases. This is consistent with the trends found in the radiative transfer models of Hartmann et al. (1994) and Muzerolle et al. (2001) who modelled the line emission from the axisymmetric magnetospheric accretion funnel flows. The line profile shapes and the strengths found here are comparable to those found in the observations (e.g. Edwards et al. 1994; Alencar & Basri 2000). However, the extent of the blue wing in the model profiles (~ -130 km s $^{-1}$ to ~ -200 km s $^{-1}$) tends to be notably smaller than a typical value found in observations (~ 300 km s $^{-1}$).

Pa β . The inclination angle dependency of the line profiles are somewhat similar to that of H β and Pa γ . The redshifted absorption component is visible at all i , and its depth slightly decreases as i increases. The extent of the line emission in the blue wing increases from ~ -130 km s $^{-1}$ to ~ -200 km s $^{-1}$ as i increases from 22°

to 60° . At $i = 22^\circ$ and 38° , the models show a classic inverse P-Cygnus profile, which is classified as Type IV R profiles according to Reipurth et al. (1996) and Folha & Emerson (2001). This consists of about 34 per cent (13 out of 37) of the objects observed by Folha & Emerson (2001). The blueshifted wind absorptions are seen at the higher inclinations ($i = 50^\circ$ and 60°), and their positions shifts towards the line centre as i increases. Similar to the H β case, the wind absorption component is located near $v \approx 0$ km s $^{-1}$ for the model with $i = 60^\circ$, and the line exhibits a double peaked shape. On contrary, the blueshifted wind component is extremely rare (1 out of 37 objects) in the observed Pa β profiles of Folha & Emerson (2001). This indicates that the Pa β line opacity in the conical-shell wind is too high possibly because the wind density and/or temperature are too high in our model.

Pa γ . The dependency on i is very similar to that of Pa β and H β . The line shows the redshifted absorption component at all i . The frequency of the redshifted absorption component is much lower (24 per cent) in the observation of ED06. A relatively strong blueshifted wind absorption appears in the higher inclination angles, i.e. $i > 50^\circ$. The peak fluxes and the profiles shapes of the models are similar to those found in the observations of 38 CTTSSs obtained by ED06, except for the blueshifted absorption feature in the models with $i > 50^\circ$. No wind absorption component is seen in the observed Pa γ profiles of ED06. As in the Pa β models, this indicates that the line opacity in the conical-shell wind is too high possibly because the wind density and/or temperature are too high in our model. The extent of the blue wing emission increases from ~ -130 km s $^{-1}$ to ~ -200 km s $^{-1}$ as i increases from 22° to 60° . This behaviour, again, is consistent with the line profile models of Hartmann et al. (1994) and Muzerolle et al. (2001).

6 DISCUSSION

6.1 Contribution to line emissions from the conical-shell wind

The model line profiles presented so far are the emergent profiles which an observer at a given viewing angle would observe. This emission consists of the emission from the inflowing gas (the accretion funnel), the outflowing gas (the wind), and the continuum emission. Although the red and blueshifted absorption components in the model line profiles could provide us some information on the physical conditions and locations of the line ‘absorption’, the locations for the line ‘emission’ could not be easily interpreted from the total emergent line profiles. For this reason, we now examine the relative contributions of the accretion funnel and the conical-shell wind to the emergent profiles by comparing the line profiles computed with (1) the accretion funnel part only, (2) the conical-shell wind only, and (3) the combination of (1) and (2). The physical parameters used for this demonstration are the same as in Model B2 (see Table 2). All the line profiles here are computed at the inclination angle $i = 30^\circ$. The results are placed in Fig. 9.

The difference in the continuum levels for each line profile is very small, i.e. the continuum emission from the wind and the accretion funnel is negligible compared to the stellar continuum; therefore, the line profiles presented in Fig. 9 use the normalized flux for the vertical scales. The figure shows that, with this particular set of model parameters, the emission in He I $\lambda 10830$ mainly arises from the accretion funnel (where the photoionization radiation is very strong); however, the emission from the wind is non-negligible, and contributing to the line centre flux. On the other hand, the wind emission in He I $\lambda 5876$ is negligibly small, and the line emission is essentially from the accretion funnel. Unlike the helium lines, the wind emission in the hydrogen lines is comparable to that of the accretion funnel for H β and Pa γ , and is significantly dominating that of the accretion funnel for H α and Pa β . However, the readers must be aware that the wind emission in hydrogen lines are very sensitive to the assumed wind temperature which is essentially controlled by our model parameter T_{\max} , as demonstrated in Section 5.1 for H α . The wind temperature in these models is approximately isothermal with $T \approx T_{\max} = 10^4$ K; however, if a slightly lower wind temperature, e.g. $T_{\max} = 8 \times 10^3$ K is used, the contribution from the wind emission will decrease significantly.

Despite the uncertainty in the wind temperature, it is interesting to note that the extent of the blue wing in some hydrogen lines, especially Pa β and Pa γ , becomes notably (~ 50 km s $^{-1}$) larger due to the wind emission. However, the amount of the blue wing extention would depend on the relative flow speed of the gas in the accretion funnel and the conical-shell wind. Since the wind emission in the hydrogen lines presented here is significant, the final emergent line profiles (computed with both wind and accretion funnel) appear broader than those from the accretion funnel or magnetosphere alone. However, this also depends on the assumed wind temperature.

6.2 Comparisons of He I $\lambda 10830$ profiles with observations

The sensitivity of He I $\lambda 10830$ to the innermost winds of CTTSs and its usefulness for probing the physical conditions of the winds have been demonstrated by e.g. ED06, Kwan et al. (2007), Kwan & Fischer (2011) and KU11. Here, we examine whether the conical-shell wind model (Model B) can account for the types of He I $\lambda 10830$ profiles seen in the observations. For this purpose, we

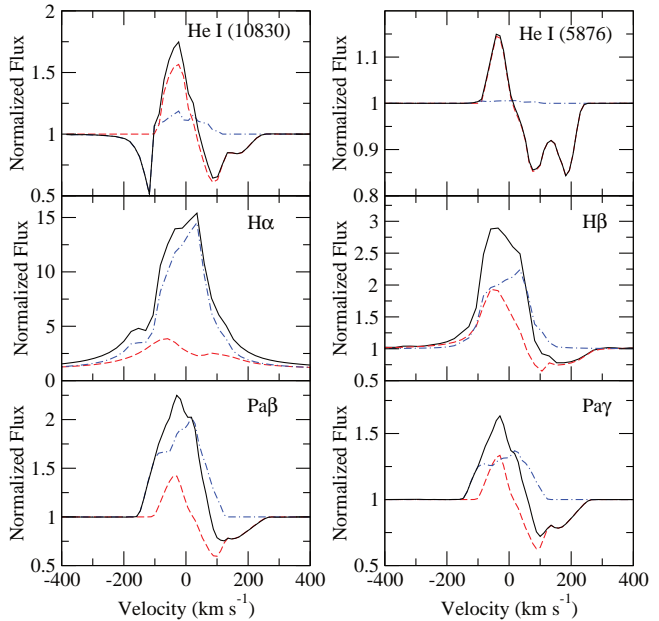


Figure 9. Comparison of the model lines profiles (He I $\lambda 10830$, He I $\lambda 5876$, H α , H β , Pa β and Pa γ) computed with different flow elements in the MHD simulation (Model B). For each line, the profiles are computed with (1) the accretion funnel part only (dash), (2) the conical-shell wind part only (dash-dot), and (3) all the flow components – the accretion funnel and the wind included (solid). The physical parameters used here are the same as in Model B2 (Table 2), and the inclination angle is $i = 30^\circ$. Note that the flux contribution from the conical-shell wind in the hydrogen lines is sensitive to the assumed wind temperature which is essentially controlled by the model parameter T_{\max} (see Section 5.1). The contribution from the wind would decrease significantly when T_{\max} is decreased.

have run a small set of line profile models for a various combinations of L_X , T_X and i while keeping other parameters fixed as in Section 5.3. We then examined if there is a resemblance between any of our model profiles to a set of He I $\lambda 10830$ line observations in ED06. In the following, we present a several example cases in which the model profile morphology is similar to that of observations.

Fig. 10 shows qualitative comparisons of the model He I $\lambda 10830$ profiles with the observation of ED06. The corresponding model parameters used are summarised in Table 3. The models shown here are not the strict fits to the observations, but rather simple comparisons of the profile morphology since we did not adjust the underlying stellar parameters (stellar masses, radii, luminosity and so on) which could be tailored to individual objects. The figure shows that the line profiles predicted from the conical-shell wind model (Model B) broadly agree with the observations. The extent of the redshifted absorption, formed in the accretion funnel flow (cf. Fig. 1), in the model line profiles is ~ 250 km s $^{-1}$, which is comparable to those in the observed profiles (~ 200 to ~ 300 km s $^{-1}$). The conical-shell wind produces a relatively narrow blueshifted absorption component in the profile in various degrees depending on the model parameters, L_X , T_X and i . As we demonstrated in the previous section (Figs. 5, 6 and 8 in Section 5), the wind absorption depths and the emission strengths are sensitive to these parameters.

A relatively strong line centre emission (as seen in the case for CY Tau) can be obtained with a relatively high X-ray luminosity ($L_X = 8 \times 10^{30}$ erg s $^{-1}$) and a relatively low inclination angle

Table 3. Summary of models used for comparison of He I $\lambda 10830$ with observations in Fig. 10.

Object	L_X (10^{30} erg s $^{-1}$)	T_X (10^6 K)	inclination ...
CY Tau	8	2	30°
CI Tau	2	2	36°
HK Tau	2	5	32°
UZ Tau W	0.4	2	30°

($i = 30^\circ$). On the hand, a relatively weak line centre emission and wind absorption (as seen in CI Tau, UZ Tau W and HK Tau) can be obtained with a relatively low X-ray luminosity ($L_X = 0.4 - 2 \times 10^{30}$ erg s $^{-1}$) and a relatively low inclination angle ($i = 30^\circ - 36^\circ$). A notable difference between the models and observation is in the extent of the blueshifted absorption component in UZ Tau W. In both cases, the observations suggest a presence of high velocity outflows (up to ~ 300 km s $^{-1}$) which cannot be explained by the conical-shell wind in our MHD model because its maximum speed is only ~ 125 km s $^{-1}$ (Fig. 2). The high velocity component seen in the observations are possibly attributed to a bipolar ‘stellar wind’ which are not implemented in our model.

As demonstrated above, the conical-shell wind model (Model B) are capable of reproducing the relatively narrow and low-velocity ($v \approx -130$ to -200 km s $^{-1}$) blueshifted absorption component in He I $\lambda 10830$ profiles. However, the model does not show the profiles with a deep and wide blueshifted wind absorption component that extends to $v \approx -300$ to -400 km s $^{-1}$, which are observed in about 40 per cent of the samples in ED09. These P-Cygni like line profiles are likely caused by stellar winds that emerge in the polar directions of CTTSs, as suggested by ED06, Kwan et al. (2007), Kwan & Fischer (2011) and KU11. The inability of our model for reproducing the P-Cygni like profile was expected since our MHD model does not include a stellar wind.

7 CONCLUSIONS

We have presented the line profile models of hydrogens and helium based on the axisymmetric MHD simulation of the outflow produced at the interface of the magnetosphere of CTTSs and their accretion discs. The so-called conical-shell wind (RO09) is formed when the stellar dipole magnetic field is compressed by the accretion disc into the X-wind like configuration. We have extended the previous conical-shell wind simulations of RO09 to include a more well defined magnetospheric accretion funnel flow which is essential for modelling the optical and near-infrared hydrogen and helium lines of CTTSs, as many of the lines show clear signs of inflow (seen as the inverse P-Cygni profiles). The formation of the well defined funnel flow with its outer radius corresponding to $\sim 2 R_\odot$ (Model B in Section 4.2) is obtained by lowering the disc density or correspondingly the mass-accretion of the disc from the previously found conical-shell wind solution of RO09 in which the magnetosphere was compressed all the way to the stellar surface by the accretion disc. The mass-accretion and mass-loss rates (in the conical-shell wind) found in the model (Model B) are $4.1 \times 10^{-8} M_\odot \text{ yr}^{-1}$ and $6.9 \times 10^{-9} M_\odot \text{ yr}^{-1}$, respectively (Table 1). The maximum velocities in the conical-shell wind and the funnel flows are ~ 125 km s $^{-1}$ (Fig. 2) and ~ 250 km s $^{-1}$, respectively. These values are all comparable to the values found in

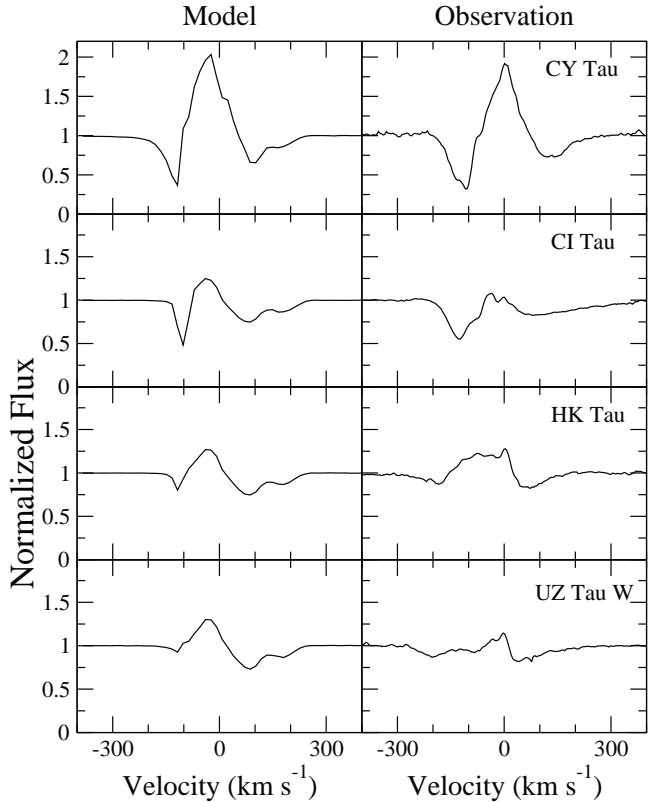


Figure 10. Qualitative comparison of the model He I $\lambda 10830$ profiles with the observation of ED06. Example model profiles (left column) are selected based on their morphological similarities with the observations (right column). For the observed profiles, the names of the objects are indicated on the upper-right corner of each panel. The corresponding model parameters used are summarised in Table 3. The He I $\lambda 10830$ profiles predicted from the conical-shell wind model broadly agree with the subset of the observations, but the model does not show a deep and wide blueshifted (P-Cygni like) profiles (not shown here) found in some CTTSs (see ED06).

observations (e.g. Hartigan et al. 1995; Gullbring et al. 1998, Calvet et al. 2000; Alencar & Basri 2000; Folha & Emerson 2001; ED06). In the following, we summarise our main findings from the line profile models based on this MHD simulation.

We find that He I $\lambda 10830$ is relatively sensitive to changes in the X-ray luminosity (L_X) and X-ray temperature (T_X) (Section 5.2). Both emission and absorption components of the line become stronger as L_X increases (Fig. 5). For a fixed L_X value, the emission and absorption components of the line become weaker as T_X increases (Fig. 6) because the peak of the thermal radiation (assumed as a single temperature gas) shifts to a higher energy and the amount of the soft X-ray emission decreases. The softer X-ray photons photoionize more He I since its photoionization cross section is larger towards the EUV frequency. The range of L_X between 4×10^{29} and 2×10^{31} erg s $^{-1}$ produces reasonable line strengths in He I $\lambda 10830$. Similarly, T_X between 2×10^6 and 2×10^7 K (with $L_X = 4 \times 10^{30}$ erg s $^{-1}$ fixed), also produced He I $\lambda 10830$ with its line strength comparable to observations. On the other hand, yet another wind sensitive line, H α , shows no significant change in its line strength when L_X and T_X are varied in the same ranges used for He I $\lambda 10830$ because the photoionization rates (in the X-ray range for H I) are small compared to the collisional rates.

A rich diversity of line profile morphology is found in our

sample hydrogen and helium model profiles (Fig. 8 in Section 5.3). Many of the model profiles are very similar to those found in the observations (e.g. Reipurth et al. 1996; Edwards et al. 1994; Muzerolle et al. 1998b; Alencar & Basri 2000; Folha & Emerson 2001; ED06). No wind absorption is seen at a very low inclination angle (e.g. $i < 22^\circ$) in any of the lines considered here. In addition, the wind absorption component seen in the higher inclination angles are rather narrow with the corresponding wind speed $v \lesssim 120 \text{ km s}^{-1}$. These suggest that the blueshifted absorption components seen in the model profiles are caused by the conical-shell wind and no significant absorption occurs (at least with the model parameters used here) in the low-density polar wind. The main shortcomings of our models are in the weakness of He I $\lambda 5876$ emission, and in the presence of the strong wind absorption component in Pa β and Pa γ which are not seen in the observations.

We have examined the relative contributions of the conical-shell wind and the accretion funnel to the hydrogen and helium line emissions (Section 6.1). We find that the conical-shell wind can significantly contribute to the line emissions in H α , H β , Pa β and Pa γ , provided that the temperature in the wind is high enough (e.g. $\sim 10^4 \text{ K}$). On the other hand, the helium lines (He I $\lambda 10830$ and He I $\lambda 5876$) have less contribution from the wind emission. The wind contribution to the hydrogen emission decreases significantly when a lower wind temperature is adopted in the profile calculations. A better constraint of wind temperatures could be obtained from the comparisons of the line ratios of e.g. the Balmer lines from observations and that from line profile models.

Using the various combinations of our main model parameters (L_X , T_X and i), we have demonstrated that the conical-shell wind model is capable of producing a subset of the line profile morphology for He I $\lambda 10830$ found in observations (Fig. 10). The model is able to reproduce a relatively narrow and low-velocity blueshifted absorption component in He I $\lambda 10830$ profiles, found in about 30 per cent of the sample in ED09, provided that the inclination angle is favourable ($\sim 30^\circ$ to $\sim 50^\circ$ for Model B, but the range will depend on the opening angle of the conical-shell wind). However, the model does not reproduce the deep and wide blueshifted wind absorption components (the P-Cygni like line profile) found in about 40 per cent of the sample in ED09. The earlier studies by Kwan et al. (2007) and KU11 demonstrated that the P-Cygni like profiles seen in He I $\lambda 10830$ of CTTSs are most likely produced by the absorption by the stellar wind that blows in the polar directions. The inability of our model for reproducing the P-Cygni like profile was expected since our MHD model did not include the stellar wind component.

Finally, in a future study, we plan to implement the stellar wind in our MHD simulations, and study its effect on the line formations, especially on the P-Cygni like profile of He I $\lambda 10830$. We also plan to investigate the line formation problems in the higher mass-accretion regimes which are somewhat similar to Model A (Fig. 1 in Section 4), and those in Königl et al. (2011) and Lii et al. (2012). These models, in which the compression of the magnetosphere toward the stellar surface is strong and the outflow due to the magnetic pressure gradient force is very strong, may be applicable to the objects during the outbursts periods such as EXors and FUORs. The time-series line profiles of the outburst can be modelled by using multiple time slices (rather than a single time slice used in this work) of MHD simulations, to study the time evolution of observed spectra.

ACKNOWLEDGEMENTS

We thank an anonymous referee who provided us valuable comments and suggestions which helped improving the manuscript. We thank Tim Harries for providing us valuable comments on the manuscript. We are grateful for Susan Edwards for providing us the observations of He I $\lambda 10830$ and Pa γ line profiles. RK would like to thank University of Nevada, Las Vegas for their hospitality during his visit. The research conducted by RK and MMR is supported by NASA grant NNX10AF63G, NNX11AF33G and NSF grant AST-1008636. Resources supporting this work were provided by the NASA High-End Computing (HEC) Program through the NASA Advanced Supercomputing (NAS) Division at Ames Research Center and the NASA Center for Computational Sciences (NCCS) at Goddard Space Flight Center.

REFERENCES

- Alencar S. H. P., Basri G., 2000, AJ, 119, 1881
- Ardila D. R., Basri G., Walter F. M., Valenti J. A., Johns-Krull C. M., 2002, ApJ, 566, 1100
- Beristain G., Edwards S., Kwan J., 2001, ApJ, 551, 1037
- Cabrit S., Edwards S., Strom S. E., Strom K. M., 1990, ApJ, 354, 687
- Calvet N., 1997, in Reipurth B., Bertout C., eds, Proc. IAU Symp. 182, Herbig-Haro Flows and the Birth of Stars. Kluwer, Dordrecht, p. 417
- Calvet N., Gullbring E., 1998, ApJ, 509, 802
- Calvet N., Hartmann L., Hewett R., 1992, ApJ, 386, 229
- Calvet N., Hartmann L., Strom S. E., 2000, in Mannings V., Boss A., Russell S., eds, Protostars and Planets IV. Univ. Arizona Press, Tucson, p. 377
- Cranmer S. R., 2009, ApJ, 706, 824
- Donati J.-F. et al., 2007, MNRAS, 380, 1297
- , 2008, MNRAS, 386, 1234
- Dupree A. K., Brickhouse N. S., Smith G. H., Strader J., 2005, ApJ, 625, L131
- Edwards S., 2007, in Bouvier J., Appenzeller I., eds, Proc. IAU Symp. 243, Star-Disk Interaction in Young Stars. Cambridge Univ. Press, Cambridge, p. 171
- Edwards S., Fischer W., Hillenbrand L., Kwan J., 2006, ApJ, 646, 319 (ED06)
- Edwards S., Fischer W., Kwan J., Hillenbrand L., Dupree A. K., 2003, ApJ, 599, L41
- Edwards S., Hartigan P., Ghandour L., Andrus C., 1994, AJ, 108, 1056
- Ferreira J., Dougados C., Cabrit S., 2006, A&A, 453, 785
- Folha D. F. M., Emerson J. P., 2001, A&A, 365, 90
- Ghosh P., Lamb F. K., 1979a, ApJ, 232, 259
- , 1979b, ApJ, 234, 296
- Ghosh P., Pethick C. J., Lamb F. K., 1977, ApJ, 217, 578
- Güdel M., Telleschi A., 2007, A&A, 474, L25
- Güdel M. et al., 2010, A&A, 519, 113
- Gullbring E., Calvet N., Muzerolle J., Hartmann L., 2000, ApJ, 544, 927
- Gullbring E., Hartmann L., Briceno C., Calvet N., 1998, ApJ, 492, 323
- Harries T. J., 2000, MNRAS, 315, 722
- Hartigan P., Edwards S., Ghandour L., 1995, ApJ, 452, 736
- Hartmann L., Avrett E., Edwards S., 1982, ApJ, 261, 279
- Hartmann L., Avrett E. H., Loeser R., Calvet N., 1990, ApJ, 349, 168

Hartmann L., Calvet N., Gullbring E., D'Alessio P., 1998, *ApJ*, 495, 385

Hartmann L., Hewett R., Calvet N., 1994, *ApJ*, 426, 669

Hartmann L., Stauffer J. R., 1989, *AJ*, 97, 873

Hirose S., Uchida Y., Shibata K., Matsumoto R., 1997, *PASJ*, 49, 193

Johns-Krull C. M., Valenti J. A., Hatzes A. P., Kanaan A., 1999, *ApJ*, 510, L41

Klein R. I., Castor J. I., 1978, *ApJ*, 220, 902

Koldoba A. V., Ustyugova G. V., Romanova M. M., Lovelace R. V. E., 2008, *MNRAS*, 388, 357

Königl A., 1991, *ApJ*, 370, L39

Königl A., Pudritz R. E., 2000, in Mannings V., Boss A., Russell S., eds, *Protostars and Planets IV*. Univ. Arizona Press, Tucson, p. 759

Königl A., Romanova M. M., Lovelace R. V. E., 2011, *MNRAS*, 416, 757

Krasnopol'sky R., Li Z.-Y., Blandford R. D., 2003, *ApJ*, 595, 631

Kurosawa R., Harries T. J., Symington N. H., 2006, *MNRAS*, 370, 580

Kurosawa R., Romanova M. M., Harries T. J., 2011, *MNRAS*, 416, 2623 (KU11)

Kurucz R. L., 1979, *ApJS*, 40, 1

Kwan J., Edwards S., Fischer W., 2007, *ApJ*, 657, 897

Kwan J., Fischer W., 2011, *MNRAS*, 411, 2383

Kwan J., Tademaru E., 1988, *ApJ*, 332, L41

Lamzin S. A., 1998, *Astronomy Reports*, 42, 322

Lii P., Romanova M., Lovelace R., 2012, *MNRAS*, 2228

Matt S., Pudritz R. E., 2005, *ApJ*, 632, L135

—, 2007, in Bouvier J., Appenzeller I., eds, *Proc. IAU Symp.*, Vol. 243, *Star-Disk Interaction in Young Stars*. Cambridge Univ. Press, Cambridge, p. 299

—, 2008, *ApJ*, 678, 1109

Muzerolle J., Calvet N., Hartmann L., 1998a, *ApJ*, 492, 743

—, 2001, *ApJ*, 550, 944

Muzerolle J., Hartmann L., Calvet N., 1998b, *AJ*, 116, 455

Orlando S., Sacco G. G., Argiroffo C., Reale F., Peres G., Maggio A., 2010, *A&A*, 510, A71

Ouyed R., Pudritz R. E., 1997, *ApJ*, 482, 712

Podio, L., Garcia, P. J. V., Bacciotti, F., et al. 2008, *A&A*, 480, 421

Pudritz R. E., Ouyed R., Fendt C., Brandenburg A., 2007, in Reipurth B., Jewitt D., Keil K., eds, *Protostars and Planets V*. Univ. Arizona Press, Tucson, p. 277

Reipurth B., Pedrosa A., Lago M. T. V. T., 1996, *A&AS*, 120, 229

Ray T., Dougados C., Bacciotti F., Eisloffel J., Chrysostomou A., 2007, in Reipurth B., Jewitt D., Keil K., eds, *Protostars and Planets V*. Univ. Arizona Press, Tucson, p. 231

Romanova M. M., Ustyugova G. V., Koldoba A. V., Chechetkin V. M., Lovelace R. V. E., 1997, *ApJ*, 482, 708

Romanova M. M., Ustyugova G. V., Koldoba A. V., Lovelace R. V. E., 2004, *ApJ*, 610, 920

—, 2005, *ApJ*, 635, L165

—, 2009, *MNRAS*, 399, 1802 (RO09)

Romanova M. M., Ustyugova G. V., Koldoba A. V., Wick J. V., Lovelace R. V. E., 2003, *ApJ*, 595, 1009

Rybicki G. B., Hummer D. G., 1978, *ApJ*, 219, 654

Sacco G. G., Argiroffo C., Orlando S., Maggio A., Peres G., Reale F., 2008, *A&A*, 491, L17

Shakura N. I., Sunyaev R. A., 1973, *A&A*, 24, 337

Shu F. H., Najita J., Ostriker E., Wilkin F., Ruden S., Lizano S., 1994, *ApJ*, 429, 781

Symington N. H., Harries T. J., Kurosawa R., 2005a, *MNRAS*, 356, 1489

Symington N. H., Harries T. J., Kurosawa R., Naylor T., 2005b, *MNRAS*, 358, 977

Takami M., Chrysostomou A., Bailey J., Gledhill T. M., Tamura M., Terada H., 2002, *ApJ*, 568, L53

Telleschi A., Güdel M., Briggs K. R., Audard M., Scelsi L., 2007, *A&A*, 468, 443

Ustyugova G. V., Koldoba A. V., Romanova M. M., Chechetkin V. M., Lovelace R. V. E., 1995, *ApJ*, 439, L39

—, 1999, *ApJ*, 516, 221

Ustyugova G. V., Koldoba A. V., Romanova M. M., Lovelace R. V. E., 2006, *ApJ*, 646, 304